GNSS Reception at the Moon: First Results of the Lunar GNSS Receiver Experiment (LuGRE)

Received: 16 September 2025 | Revised: 27 November 2025 | Accepted: 5 January 2026

DOI: 10.33012/navi.756

ORIGINAL ARTICLE

GNSS Reception at the Moon: First Results of the Lunar GNSS Receiver Experiment (LuGRE)

Joel J. K. Parker*[1] | Fabio Dovis*[2] | Lauren Konitzer[1] | Nathan Esantsi[1] | Benjamin Ashman[3] | Alex Minetto[2] | Andrea Nardin[2] | Oliviero Vouch[2] | Simone Zocca[2] | Fabio Bernardi[4] | Matilde Boschiero[4] | Samuele Fantinato[4] | Efer Miotti[4] | Claudia Facchinetti[5] | Mario Musmeci[5] | Giancarlo Varacalli[5]

[1] NASA Goddard Space Flight Center, Greenbelt, MD, USA

[2] Dept. of Electronics and Telecommunications, Politecnico di Torino, Turin, Italy

[3] NASA Headquarters, Washington, DC, USA

[4] Qascom S.r.l., Cassola, Italy

[5] Agenzia Spaziale Italiana (ASI), Rome, Italy

Correspondence
*Joel J. K. Parker
Email: joel.j.k.parker@nasa.gov
Fabio Dovis
Email: fabio.dovis@polito.it

Abstract

This article presents a comprehensive overview of the successful execution of the Lunar GNSS Receiver Experiment (LuGRE), the first known demonstration of global navigation satellite system (GNSS) signal acquisition, tracking, and navigation near and on the Moon. A general overview of the mission, payload, and ground system is provided. The as-flown mission profile is described in detail across the Earth–Moon transit, low lunar orbit, and lunar surface phases. A description of the high-level results of the mission is presented, including an evaluation of C/N_0, the quality of the pseudorange and carrier-phase measurements, the signal availability, the results of real-time least-squares position, velocity, and time estimation by the onboard receiver, and an evaluation of the in-phase and quadrature samples captured during the mission. Finally, key observations for future lunar GNSS users are discussed. The article also serves as a reference guide to the unique open data set released by the project.

Keywords

Blue Ghost Mission 1 (BGM1), Commercial Lunar Payload Services (CLPS), Firefly Aerospace, Galileo, GNSS, GPS, Lunar GNSS Receiver Experiment (LuGRE), lunar navigation, lunar PNT, space service volume

1 | INTRODUCTION

The Lunar GNSS Receiver Experiment (LuGRE) is the first known demonstration of Earth-based global navigation satellite system (GNSS) signal acquisition, tracking, and navigation at the Moon. LuGRE builds on nearly 30 years of development of high-altitude use of a GNSS in space, extending from the initial experiments of Falcon Gold (Powell et al., 1999) and Equator-S (Balbach et al., 1998) in the late 1990s through operational use of the Global Positioning System (GPS) by the National Aeronautics and Space Administration (NASA) Magnetospheric Multiscale (MMS) mission at nearly 50% lunar distance starting in 2017 (Winternitz et al., 2017). Awareness of these methods has increased alongside development of the technology, including adoption of the first formal definition

of the space service volume by the GPS program in 2006 (Bauer et al., 2006) and publication of The Interoperable GNSS Space Service Volume by the International Committee on GNSS (ICG) in 2016 (United Nations Office for Outer Space Affairs, 2021). The history of weak-signal GNSS has been extensively recounted by Ashman et al. (2018).

In parallel with these developments has been the renewed focus on lunar exploration by global space agencies. This focus is documented by the International Space Exploration Coordination Group (ISECG) in its series of Global Exploration Roadmap reports, which now document dozens of planned launches to the Moon in the coming decades by numerous independent actors (ISECG, 2024). Technology needs for these missions are increasing as well, with calls for 100-m-class or better positioning on the lunar surface and real-time, onboard formulation of positioning, navigation and timing (PNT) solutions with near-continuous availability (Ashman et al., 2021).

A burgeoning body of work in the literature proposes that a GNSS can provide valuable contributions to advanced lunar-vicinity PNT, especially in the cislunar transit phase between the Earth and Moon and during lunar orbit and surface phases with clear Earth visibility (Konitzer et al., 2024; Winternitz et al., 2019). Given the need for high-gain antennas (HGAs) to receive the signals and limitations in the geometric diversity of signals traveling from the Earth's vicinity, for many applications, a GNSS is likely to be used as part of a combination of navigation methods tailored to the distinct phases of a particular mission (Delépaut et al., 2020), for example, contributing to overall PNT knowledge during transit and in lunar orbit as a primary observable and then augmenting methods such as optical navigation and relative navigation during high-dynamic real-time operations when accuracy needs are more demanding.

Space agencies are responding to the projected increase in utilization and capability needs. This includes the China National Space Administration (CNSA), European Space Agency (ESA), Indian Space Research Organisation (ISRO), Japan Aerospace Exploration Agency (JAXA), Korea AeroSpace Administration (KASA), and NASA, all of which have expressed interest in developing lunar-vicinity PNT systems providing services locally to lunar users. Together, NASA, ESA, and JAXA have begun development of the LunaNet framework, which seeks to define (among other things) the protocols and elements needed to provide a common set of PNT signals that can be used interoperably and transparently from independent providers (Israel et al., 2020). Similarly, CNSA has outlined plans to provide lunar-targeted PNT signals from both Earth orbit and from platforms in lunar and cislunar space (Jiang, 2025), and ISRO and KASA have each discussed plans for lunar orbital or surface beacon systems (Joo, 2025; Shukla, 2025). To support these developments, the ICG established its Working Group on Lunar PNT in 2024 and in 2025 initiated an annual series of cislunar PNT workshops with the Interagency Operations Advisory Group, aiming to consolidate the rapid developments in this field for the broader community.

A GNSS has the potential to contribute to and augment these future PNT systems—both as a provider of PNT for the transmitting vehicles, which supports their ability to then deliver precise PNT signals to users, and as a direct source of PNT knowledge for users who may also utilize a range of other services in a multi-source, fused navigation system. First, however, capable operational lunar GNSS user equipment must be available, which requires that the fundamental feasibility of lunar-vicinity GNSS-based navigation be demonstrated.

LuGRE was envisioned and developed as this initial demonstration step, aiming to provide a stepping stone to future development of lunar-vicinity and cislunar

GNSS and next-generation dedicated lunar PNT systems. Following LuGRE, Lunar Pathfinder will fly a second, independent test of GNSS reception in lunar orbit (Giordano et al., 2022), and others may perform their own demonstrations in the coming years. Together, the cumulative data sets from these missions will establish the foundation of knowledge for a GNSS at the Moon, fulfilling the vision established by the early pioneers of high-altitude spaceborne GNSS.

This paper outlines the background, technology, and results of the LuGRE mission. Section 2 presents an overview of the mission along with its objectives, requirements, and concept of operations. Section 3 presents details of the payload and ground systems used during the flight. Section 4 outlines the as-flown operations and data collection. Section 5 provides a summary of the results of the mission, including signal strength, measurement quality, signal availability, and navigation estimation. Section 6 presents observations and findings from the overall mission experience for future mission developers to consider. Finally, Section 7 provides conclusions, and Section 8 discusses the public data set.

2 | MISSION OVERVIEW

LuGRE is a joint NASA–Italian Space Agency (ASI) payload, developed to extend GNSS-based navigation and timing to the Moon, on the Blue Ghost Mission 1 (BGM1) lunar lander built by Firefly Aerospace. LuGRE flew as one of 10 NASA-funded payloads on the Firefly BGM1 lander, awarded via the NASA Commercial Lunar Payload Services (CLPS) Task Order 19D. BGM1 launched January 15, 2025, successfully landed on the lunar surface on March 2, 2025, and completed its mission on March 16, 2025, at the end of the lunar day.

The primary organizations involved include NASA via its Space Communication and Navigation Program, ASI, Qascom S.r.l., and Politecnico di Torino via its Department of Electronics and Telecommunications. Qascom led the development and testing of the payload system, including in-house development of the LuGRE GNSS receiver. Politecnico di Torino led ASI science activities as co-principal investigator with NASA. NASA and ASI jointly managed the project, with ASI responsible for all activities related to the Qascom payload and for coordinating the scientific contributions of Politecnico di Torino. NASA was responsible for overall integrated project management, systems engineering, and programmatic and integration activities with CLPS and Firefly. All four organizations jointly operated the payload and performed scientific and data processing activities after mission completion.

The LuGRE project began in mid-2020, included as one of 10 NASA payloads in the CLPS 19D request for task order proposals. The flight was awarded to Firefly in early 2021, initiating a rapid sequence of LuGRE development milestones, including a system requirement review in May 2021, critical design review in August/September 2021, and payload-level integration and test (I&T) activities beginning shortly after and extending through 2022. The LuGRE payload was delivered to Firefly in February 2023 and was later integrated on the lander in advance of lander-level I&T and launch preparation activities.

LuGRE was developed as a NASA do-no-harm class payload, meaning that its only requirement for mission success was to not harm the lander system and other payloads—in effect acting as an on-orbit test of the payload system, consistent with its scope as a technology demonstration. For scientific success, three scientific objectives were defined, as follows:

OBJECTIVE 1 Receive GNSS signals at the Moon. Return data and characterize the lunar GNSS signal environment.

TABLE 1
LuGRE Top-Level Scientific Requirements

ID	Title	Requirement
L101	GNSS measurements	*Baseline*: The LuGRE project shall receive and downlink GNSS measurements from the GPS L1 C/A and L5 signals and from the Galileo E1 OS and E5a signals at the Moon. *Threshold*: The LuGRE project shall receive and downlink at least one type of GNSS measurement from any of the GPS L1 C/A, GPS L5, Galileo E1 OS, or Galileo E5a signals at the Moon.
L102	Lunar navigation demonstration	*Baseline*: The LuGRE project shall demonstrate real-time GNSS-based navigation in transit beyond 30 RE from Earth and on the lunar surface. *Threshold*: The LuGRE project shall demonstrate GNSS-based navigation in transit beyond 30 RE from Earth or on the lunar surface using payload-collected data.

OBJECTIVE 2 Demonstrate navigation and time estimation using GNSS data collected at the Moon.

OBJECTIVE 3 Utilize collected data to support the development of GNSS receivers specific to lunar use.

From these objectives, two top-level scientific requirements were derived, as shown in Table 1. Here, the "baseline" requirement is the full requirement that LuGRE was designed to meet, whereas the "threshold" requirement captures the minimum performance needed for scientific success. The objectives and scientific requirements were further developed into an extensive scientific plan, as outlined by Konitzer et al. (2024).

The overall concept of operations is illustrated in Figure 1. The LuGRE receiver was designed with modes to produce real-time GNSS observables (e.g., C/N_0, pseudorange, Doppler, carrier phase), real-time navigation solutions, and raw baseband in-phase and quadrature (I/Q) samples, enabling both onboard and ground processing approaches to meet the objectives and requirements. The opportunity to obtain raw GNSS observables and signal samples was intentionally included to address the specific mission objectives, as these data enable capabilities beyond standard onboard position, velocity, and time (PVT) products—specifically, in-flight troubleshooting, extended scientific analyses, and post-mission studies, thereby broadening both operational and research potential (Fiorina et al., 2025; Nardin et al., 2022, 2023; Sciacca et al., 2025; Vouch, Nardin, Minetto, Zocca, Dovis, et al., 2024; Vouch, Nardin, Minetto, Zocca, Valvano, & Dovis, 2024).

The primary phases of the mission were post-launch commissioning, transit operations in the Earth phasing loops and in lunar orbit, and post-landing surface operations. During commissioning and transit, the LuGRE HGA was locked in the horizontal outward-facing position, and pointing was achieved by reorienting the entire BGM1 lander. Operational periods were limited in number and duration to preserve lander attitude control resources; a minimum of 15 periods of 1 h each were baselined and distributed across commissioning, Earth phasing orbits, and lunar orbits. Each period could be used for a combination of real-time signal tracking and PVT processing and for short I/Q sample captures (SCs).

LuGRE was turned off during powered descent and began operations on the lunar surface when the HGA platform could be deployed and pointed to track the Earth, enabling continuous observations and increased data volume to

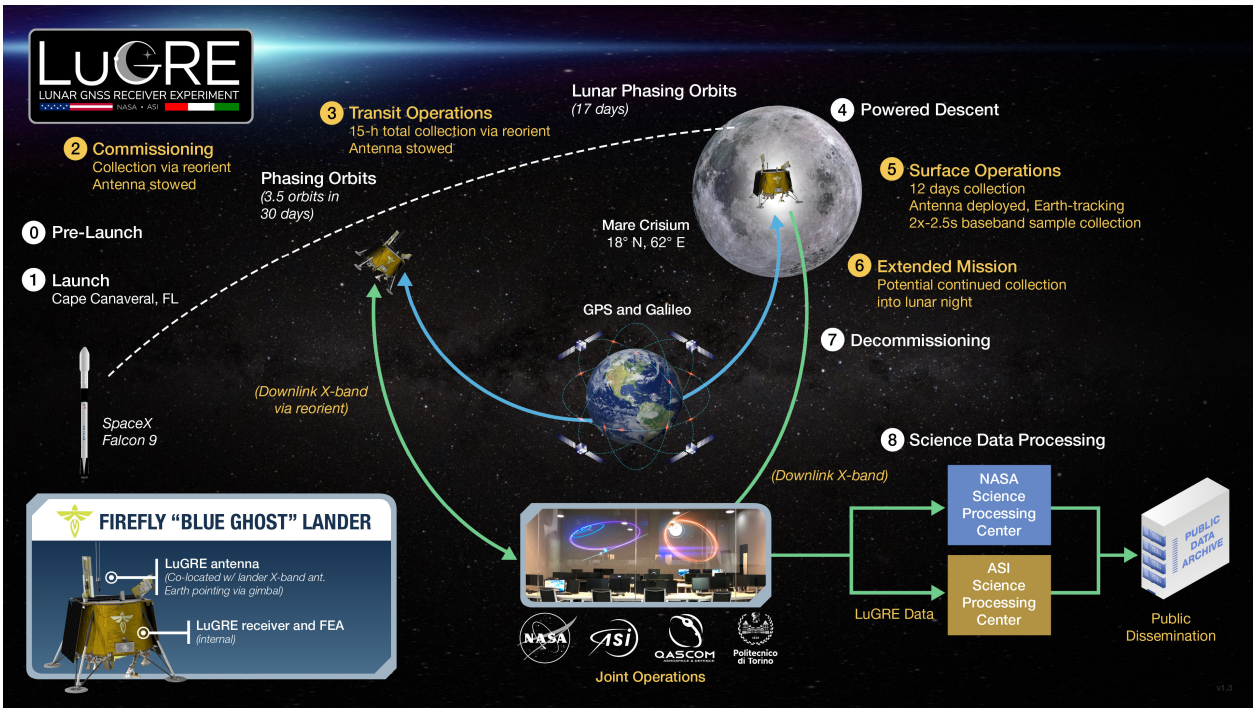

FIGURE 1 LuGRE pre-flight concept of operations

support two extended I/Q SC operations. The surface phase was planned to last 12 Earth days (one lunar day), after which the lander and payload would lose power, marking mission completion. During the operational periods, data were downlinked to Firefly and distributed to the LuGRE Payload Operations Center (POC) to support joint NASA–ASI operations. After the operational mission, a 6-month science processing period was initiated, followed by public release of the LuGRE data products in October 2025. The as-flown operations and data collection are discussed in Section 4, and the data products are discussed in Section 8.

3 | SYSTEM ARCHITECTURE

The LuGRE system consists of a payload flown onboard the Firefly BGM1 lunar lander and a distributed ground segment necessary to operate the payload. Section 3.1 describes the hardware and software design and implementation of the payload, while Section 3.2 describes the ground segment architecture and operational cadence.

3.1 | Payload

The LuGRE hardware was designed to support the top-level scientific requirements described in Section 2 while also satisfying the do-no-harm requirement as a payload hosted on the BGM1 lander. The design prioritized robustness, adaptability, minimal mass, and power efficiency, which allowed LuGRE to withstand the severe challenges of the deep space environment (Fantinato et al., 2022, 2025; Pulliero et al., 2023). The LuGRE payload development process resulted in

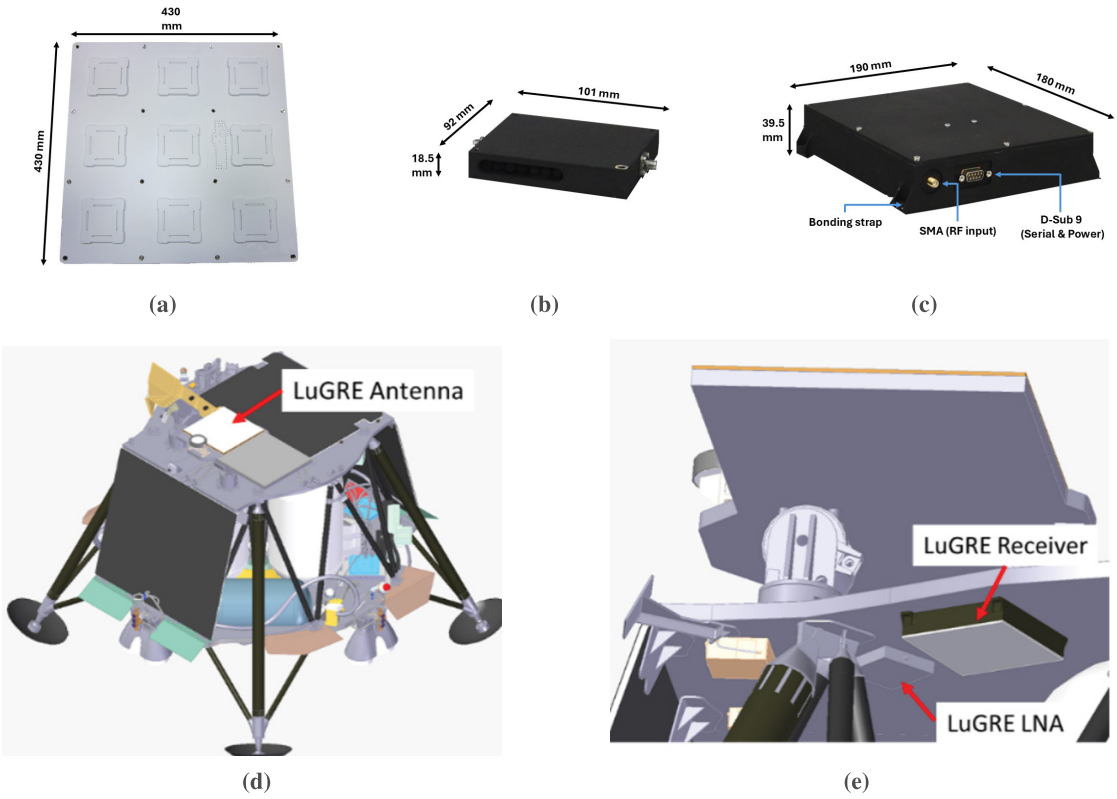

FIGURE 2 LuGRE hardware components and their relative locations on the BGM1 lander. (a) LuGRE HGA, (b) LuGRE LNA, (c) LuGRE receiver, (d) Location of the LuGRE HGA on the BGM1 lander. The NGLR payload is just above the LuGRE HGA on the same panel. Image: Firefly Aerospace, (e) Location of the LuGRE receiver and LNA below the top deck of the BGM1 lander. Image: Firefly Aerospace.

a flight model with a total mass of less than 5 kg and a maximum operational power of 14 W.

The LuGRE payload combines several custom hardware components. These components and their locations on the BGM1 lander are shown in Figure 2 and are described in detail in the following sections.

3.1.1 | *High-Gain Antenna*

The LuGRE HGA was designed to operate in both the L1/E1 and L5/E5a GNSS bands. It was designed as a 3×3 planar right-hand circularly polarized passive L-band antenna with a high gain and directive main-lobe. The resulting antenna design achieved a peak boresight gain of 15.35 dBic and 12° half-power beamwidth in L1/E1 and 14.56 dBic and 16° half-power beamwidth in L5/E5. Figure 3 depicts the antenna gain patterns measured in the NASA Goddard Space Flight Center (GSFC) anechoic chamber as a standalone component, mounted on a mockup panel with an integrated model of the neighboring Next-Generation Lunar Retroreflector (NGLR) payload. Additionally, the HGA contained an integrated notch filter to limit the contributions of out-of-band interference. The HGA was mounted on a gimballed platform on the top deck of the lander, adjacent to the lander's X-band communications antenna and the NGLR payload on the same platform, as shown in Figure 2(d).

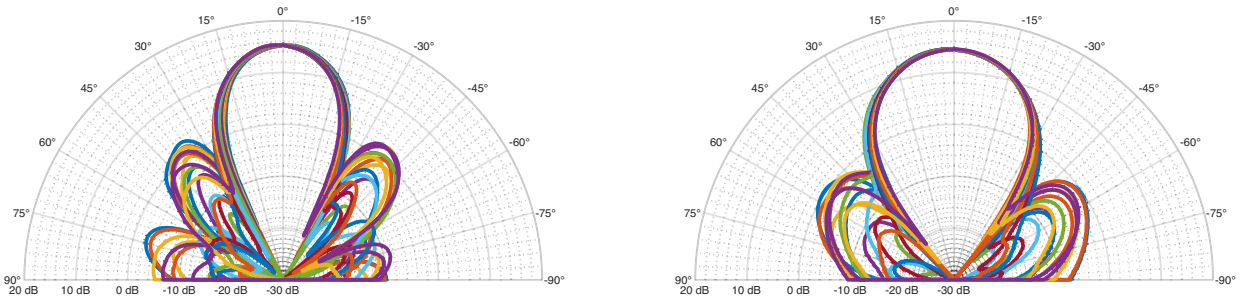

FIGURE 3 Measured HGA gain patterns in LuGRE receive bands. (a) L1/E1, (b) L5/E5a. Patterns are shown as gain (radial) over elevation (angular) at 10° azimuthal cuts (individual traces).

3.1.2 | *Front-End Assembly*

To amplify the signals received by the HGA, a dual-frequency front-end assembly (FEA) was employed, containing a pre-selection band pass filter, followed by a low-noise amplifier (LNA) and an equalizer. As shown in Figure 2(e), the FEA was mounted under the lander's deck and directly connected to the HGA via a space-qualified coaxial harness. The distance between the FEA and the HGA was minimized to reduce the loss before the LNA.

The LNA was designed to be selective around the L1 and L5 bands, amplifying incoming signals while mitigating out-of-band contributions and noise. The use of custom resonance filters resulted in a measured gain of 41.5 dB in L1/E1 and 44.2 dB in L5/E5, with better than 70-dB isolation outside the passband. The LNA noise figure was measured to be 0.8 dB in L1 and 1.3 dB in L5.

3.1.3 | *QN400-SPACE GNSS Receiver*

The heart of the LuGRE payload was Qascom's multi-constellation and multi-frequency QN400-SPACE GNSS receiver. The receiver hardware and software were informed by designs previously tested on several flights such as the UP Aerospace SL-14 and SL-15 sounding rockets (Guzzi et al., 2025) and the Bobcat-1 CubeSat (Croissant et al., 2021) and were further refined for high-sensitivity acquisition in deep space (Fantinato et al., 2022; Pulliero et al., 2023). The resulting receiver properties flown for the LuGRE mission are summarized in Table 2.

The receiver was designed in a dual cold-redundant configuration managed by an integrated supervisory board. The supervisory board controlled the selection of two identical GNSS receiver modules (RXA as the primary and RXB as the secondary), providing robustness against single-event-latchup events as well as monitoring and mitigation of potential over-current scenarios. The receiver contained a Xilinx Zynq 7000 SoC baseband processor and an Analog Devices AD9361 front-end to capture and digitally process radio frequency (RF) signals. Additionally, software-defined radio technology allowed for software re-configurability and a high degree of signal processing flexibility. This included the ability to configure receiver settings and perform full or partial software updates through telecommands generated and uploaded from the ground.

The high-sensitivity GNSS performance of the receiver was based on Qascom's proprietary acquisition and tracking logic specifically designed for the mission, combining coherent and non-coherent accumulation strategies

TABLE 2
Summary of LuGRE Receiver Design Properties

Parameter	Value/Properties
Physical Properties	
Mass	1.24 kg
Power	< 14 W (maximum operating)
Envelope	$(19.0 \times 18.0 \times 3.95)$ cm
Operating Temperature Range	-35°C to 50°C
Signal Reception	
Constellations and Bands	GPS L1 C/A and L5; Galileo E1BC and E5a
Signal Acquisition Threshold	23 dB-Hz
Signal Tracking Threshold	20 dB-Hz
Acquisition Strategy	L1/E1-first
Software Capabilities	RTP mode: PVT via weighted least squares; POD via extended Kalman filter SC mode: I/Q snapshots Assistance data from ground: GNSS broadcast ephemeris and filter aiding parameters
Telemetry Types	ACQ - contains information on acquired satellites, Doppler, and correlators RAW - contains pseudorange, Doppler, carrier phase, and C/N_0 NAV - contains PVT solutions in Earth-centered Earth-fixed frame POD - contains navigation filter solutions in Earth-inertial frame (EME2000) IQS - contains I/Q sample batches
External Interfaces	RF - SMA female connector Serial (RS-422) - telemetry/telecommand interface through a DSub-9 connector Power - DSub-9 connector, 28 V

(Fantinato et al., 2025; Tedesco et al., 2023). Moreover, the receiver used a warm-start approach, exploiting aiding data uploaded from the ground and received by the lander. The real-time processing (RTP) mode produced instantaneous real-time PVT navigation solutions (when a sufficient number of signals was available, referred to as NAV telemetry) via a weighted least-squares estimator initialized with *a priori* predicted lander trajectory information. Similarly, navigation filter solutions (referred to as POD telemetry) were obtained using a custom extended Kalman filter implementation. An additional receiver mode, SC mode, allowed for capture of snapshots of raw signals as I/Q samples (IQSs) for post-processing on the ground, referred to as IQS telemetry. The parameters of the captured IQS packets were configurable via telecommand.

The receiver architecture distributed a frequency reference from an integrated internal oscillator to the FEA and field programmable gate array. The oscillator used was a commercial-grade voltage-controlled temperature-compensated crystal oscillator (VCTCXO), with stability properties measured at ambient conditions shown in Figure 4. Notably, the oscillator was observed to exhibit significant transient clock drift behavior upon power-on. An example of the receiver clock drift start-up transient, typically lasting 10–15 min, is shown in Figure 5, as estimated by the receiver during a representative commissioning operation.

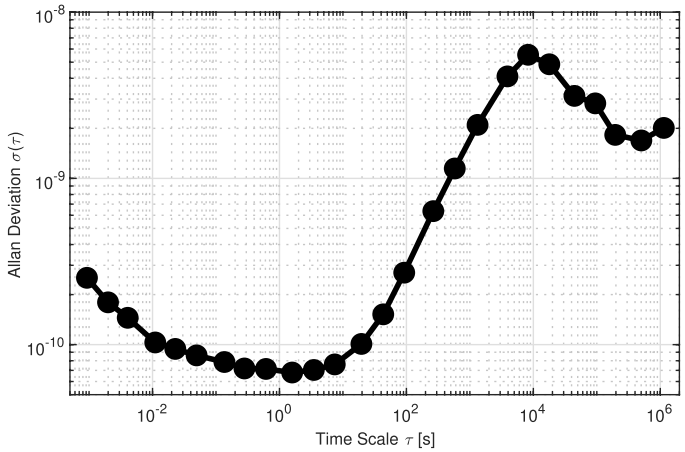

FIGURE 4 Measured Allan deviation for the internal VCTCXO at ambient temperature

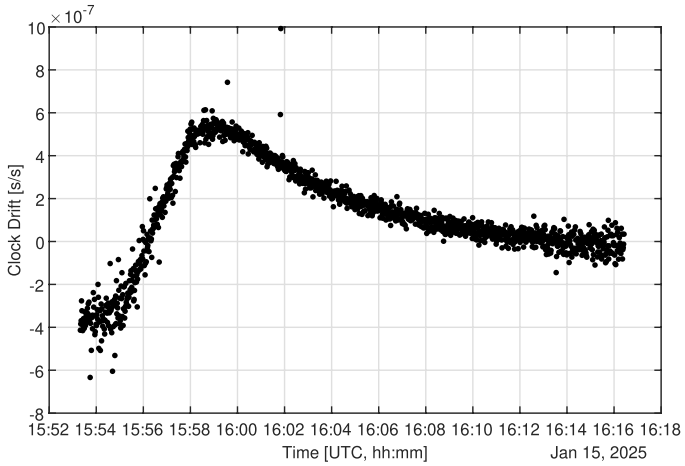

FIGURE 5 Example of start-up clock drift transient observed in-flight, estimated as part of the receiver PVT solutions

3.2 | Ground System and Operations

The LuGRE project involved the development of both flight and ground segments. The LuGRE ground system was designed as a geographically distributed architecture involving NASA GSFC in Greenbelt, Maryland, USA; ASI in Rome, Italy; Qascom in Bassano del Grappa, Italy; and Politecnico di Torino in Turin, Italy. The components of the ground system and its external interfaces are shown in Figure 6 and are described in the following paragraphs.

Payload Operations Center (POC) (NASA GSFC) was the LuGRE payload operational authority and was responsible for monitoring the LuGRE payload, ensuring its safety, and delivering telecommands to the Mission Control Center (MCC). It also provided the point of contact for Firefly and NASA CLPS. The POC processed Firefly predictive data provided by the MCC as detailed in the "Aiding" paragraph below, performed the final step of the telecommand verification process, and led the payload operations planning cycle. The POC contained the Science Processing Center, which led scientific activities during operations and continued post-mission for data analysis and public product generation.

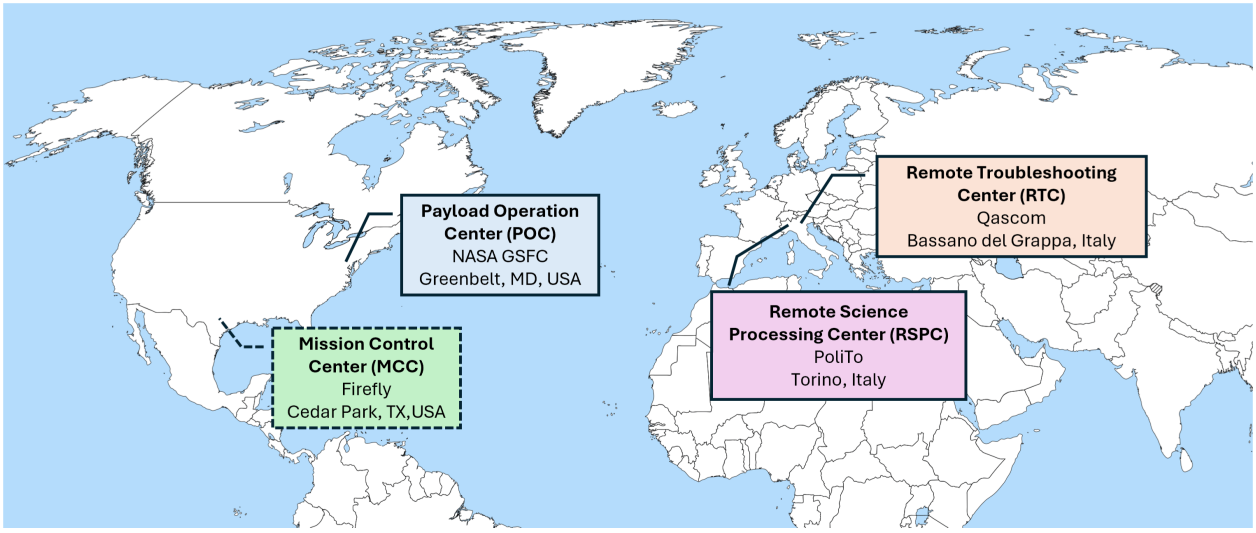

FIGURE 6 LuGRE ground system components (solid lines) and external interfaces (dashed lines)

Remote Troubleshooting Center (RTC) (Qascom) was the LuGRE payload technical authority. The RTC generated, tested, and verified the telecommands to be provided to the receiver and processed downlinked receiver telemetry to verify consistency and to evaluate performance. The RTC developed all major software used for command validation simulation and troubleshooting and to support the operational activities through all phases. It also acted as a redundant control center for the POC, implementing all of the critical functions needed to support payload operations if needed.

Remote Science Processing Center (RSPC) (Politecnico di Torino (PoliTo), Department of Electronics and Telecommunications) was responsible for performing quick-look scientific evaluations of the payload telemetry, supporting the science team in the POC with payload telemetry analysis, and supporting the payload operations planning cycle through analysis to maximize the performance of upcoming operations. The RSPC also developed the LuGRE quick Navigation Analysis and Reporting Tool (LuNART-q) to deliver early assessments of the scientific integrity of received payload data to the POC via an Operation Summary Report and to evaluate POC-provided simulations via a Prediction Evaluation Report (Minetto et al., 2025).

Firefly Mission Control Center (MCC) (Cedar Park, Texas, USA) operated the BGM1 lander and was the primary external interface for LuGRE payload operations. The MCC was responsible for delivering payload commands to the lander for execution, returning payload and lander telemetry, managing the overall operation schedule, and providing voice communications between LuGRE and the BGM1 operators.

The following main activities were performed before, during, and after each operation, as illustrated in Figure 7:

Planning The operation planning process was active in the days prior to each operation. LuGRE and Firefly utilized a baseline operation schedule developed pre-launch as the basis for scheduling the payload activities. As the flight developed, Firefly readily accommodated changes to the baseline plan

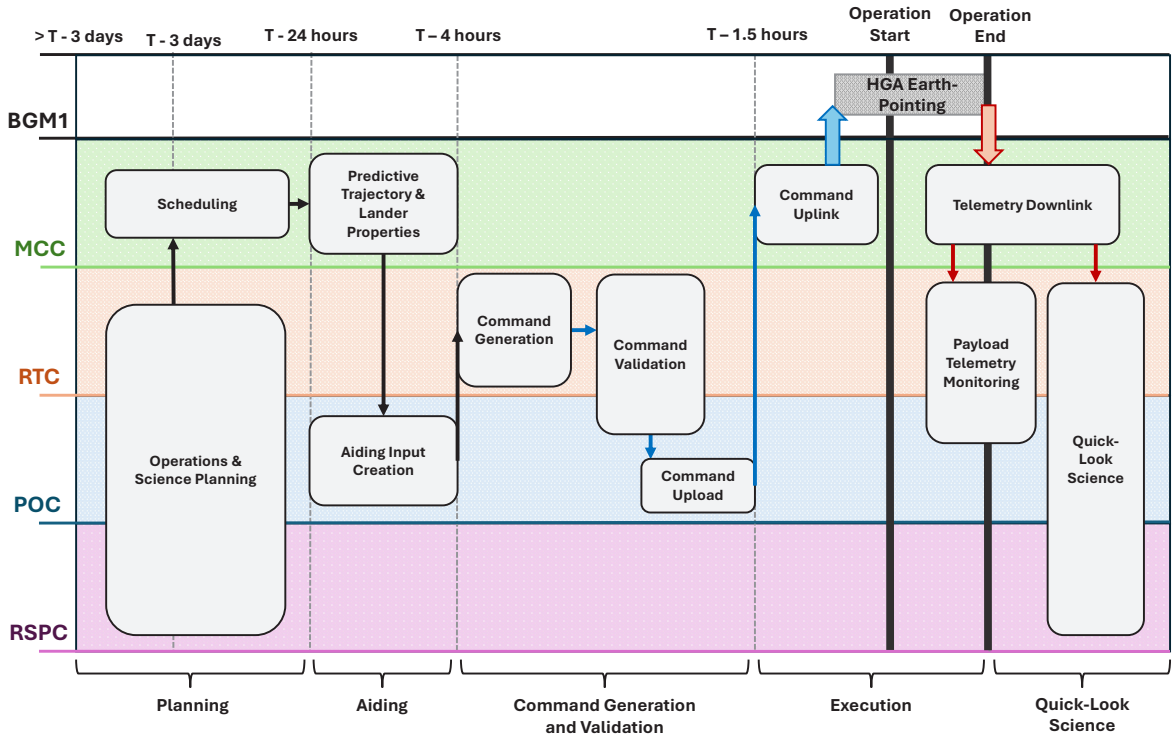

FIGURE 7 Flow diagram of LuGRE operations
Colored arrows indicate the flow of preparatory data (black), commands (blue), and telemetry (red).

as needed to respond to lander-level activities, e.g., schedule keep-outs, and to improve scientific value to LuGRE within the constraints of the overall mission-level operations. The LuGRE ground system retrieved GNSS broadcast ephemeris information from the Crustal Dynamics Data Information System (CDDIS) for GPS and the Time and Geodetic Validation Facility (TGVF) for Galileo.

To support the scientific side of the planning process, the LuGRE team simulated upcoming operations using the Goddard Enhanced Onboard Navigation System (GEONS) and its GEONS Ground Matlab Simulation (GGMS) front-end to predict the availability and signal strength (C/N_0). GEONS has an extensive history of use by multiple missions as an in-flight navigation filter and via GGMS as a ground tool for visibility simulation and navigation analysis (Ashman et al., 2024; Winternitz et al., 2019). Starting several days in advance, the POC produced simulations of signal availability and C/N_0 for upcoming operations. At daily planning meetings, the team selected the operation start time and the start times and durations of the SC and RTP modes to maximize (i) the likelihood of acquisition of strong L1/E1 signals early in the window, (ii) the total data volume and/or likelihood of tracking multiple unique signals, and (iii) the signal content of IQS batches. These selections were then coordinated with Firefly for scheduling.

Aiding The LuGRE receiver was used in warm start, exploiting three types of aiding information at start-up: time (provided by the lander within approximately 100 ms of Coordinated Universal Time [UTC]), GNSS broadcast ephemerides, and POD filter aiding information including (i) predictive

trajectory, (ii) Earth orientation parameters, and (iii) lander physical parameters. Firefly delivered the predicted trajectory and lander information at 24 h prior to each operation, and the POC processed this information into an aiding input delivery to the RTC for inclusion in payload commands. The broadcast ephemerides, from CDDIS for GPS and TGVF for Galileo, were pulled within 2 h of the operation start time to maximize the accuracy of the ephemeris data.

Command Generation and Validation After delivery of the aiding data from the POC, the RTC validated the data using internal tools and then generated receiver telecommand files consisting of the aiding information and the receiver configuration necessary to collect the desired scientific information. The RTC validated the generated telecommands in a testbed using a Spirent GNSS simulator and the LuGRE flight-spare receiver unit to verify accuracy and consistency with respect to the desired operation. Once validated, the RTC delivered the telecommand files to the POC for a final verification and validity check using a Firefly-provided lander interface simulator. Once finalized, the POC delivered the command files and associated execution commands to the MCC, before a Firefly-dictated cutoff time. For long-duration operations during the surface phase, updated broadcast ephemeris commands were additionally generated every 2 h and provided to Firefly for upload at the next opportunity.

Execution In the minutes prior to an operation, the MCC uplinked the payload command files to the lander for staging and commanded the lander to slew (in transit) or gimbal (during surface operations) the antenna platform to an attitude that pointed the LuGRE HGA to the Earth. During the execution of the operation, the MCC downlinked telemetry from the lander for retrieval by the POC and RTC. During each operation, the POC monitored the status in real time using a Firefly-provided telemetry dashboard showing health and status metrics (e.g., current, temperature, data received), whereas the payload telemetry was ingested into a custom Grafana dashboard developed for the mission and accessible to all LuGRE ground sites.

Quick-Look Science After completion of the operation, the RSPC used the purpose-built LuNART-q quick-look science tool to perform a preliminary evaluation of the receiver telemetry, including C/N_0, GNSS observables, PVT and precise orbit determination (POD) solutions, and evaluation of any IQS collections. The RSPC augmented LuNART-q with other tools to perform deeper analysis and to assist with the evaluation of predictions and specific observations as needed. The RTC independently produced a technical evaluation report of receiver status and performance; both evaluations were presented at the daily planning meeting to evaluate the performance of the prior operation and to assist in the planning of upcoming operations.

This flow of activities was necessarily flexible, with exceptions and additional iterations occurring as lander events required, particularly during longer-duration operations on the lunar surface.

4 | IN-FLIGHT OPERATIONS AND DATA COLLECTION

BGM1 launched on January 15, 2025, at 06:11 UTC into its Earth–Moon transit trajectory, consisting of 3.5 phasing loops from launch to lunar orbit insertion (LOI)

and continuing with a lunar orbit phase until the initiation of powered descent. LuGRE and Firefly planned a sequence of 15 1-h operation windows during the overall transit phase—10 from launch to LOI1 and 5 in lunar orbit. Figure 8(a) shows the as-executed sequence of activities, including lander maneuvers (e.g., apogee 1 maneuver [A1M], perigee 1 maneuver [P1M], trans-lunar injection [TLI], etc.) and LuGRE operations (OP1_0, OP2_0, OP3_0, etc.). The LuGRE operations were identified by a sequential numeric ID based on the pre-flight plan, including placeholders for backup and secondary opportunities; thus, the as-executed sequence is not continuously numbered. Pre-flight planned operations were marked as "OP*n*_0." New operations inserted into the baseline plan were marked as "OP*n*_1," where *n* is the previously executed sequential ID.

Two operational modes were available: SC mode, in which raw I/Q baseband signal samples were recorded, and RTP mode, in which the receiver would perform acquisition, tracking, and navigation. The majority of operations were mixed-mode, in which both modes were executed in sequence.

In the first phasing loop, LuGRE executed two commissioning operations (OP1_0 and OP2_0) within the first 24 h of the mission, both with altitudes under 30 Earth radii (RE), followed by the first science operation (OP3_0) near 40-RE altitude approximately 24 h later, and finally OP5_0 (51 RE) minutes after the A1M lander maneuver. Altitude measurements in units of RE are referenced to the Earth geoid at the start time of each operation, where 1 RE is equal to 6378.137 km. In the second and third phasing loops, LuGRE executed several operations seeking to acquire and track signals at various distances from Earth; these included OP9_0 at 35 RE, OP12_0 at 40 RE (matched to OP3_0), OP14_0 at 30 RE, OP17_0 at 45 RE, OP18_0 at 50 RE (matched to OP5_0), OP21_0 at 33 RE, and finally OP22_0 at 55 RE, just before LOI1.

Additionally, during this phase, a special operation labeled OP4_1 was executed between OP3_0 and OP5_0 without pointing the LuGRE antenna toward the Earth. This operation was performed to provide an in-flight I/Q SC of any electrogmagnetic interference (EMI) present in the LuGRE receive bands. A characterization of I/Q SC data from the mission is discussed in Section 5.5.

After successful lander execution of LOI1, the lander spent 4 days in a 100- to 6000-km-high lunar orbit prior to the apoapsis-lowering LOI2. LuGRE executed OP23_0 in the first lunar orbit after LOI1, at an Earth altitude of over 62 RE, marking the first GNSS reception in lunar orbit. After LOI2, the lander entered two similar low lunar orbit periods, both with periapsis slightly over 100 km and apoapsis under 200 km. LuGRE executed four operations in this period, including the farthest in-flight operation (OP27_0) at more than 63 RE from Earth's surface.

BGM1 landed successfully on March 2, 2025, at 08:34 UTC, beginning the lunar surface phase of the mission, as illustrated in Figure 8(b). LuGRE powered on less than 24 h later and executed two extended-duration operations: OP38_0 for 24 h followed by OP40_0 for nearly 13.5 h, at which time the lander entered a period of high heating as it approached lunar noon and LuGRE payload operations were temporarily paused until temperatures cooled sufficiently. A special feature of the BGM1 mission was a lunar eclipse occurring March 14, which induced rapid thermal changes, similar to a back-to-back sunset and sunrise. LuGRE executed OP73_0, an extended SC, just after eclipse end, followed by OP74_0 for 24 h and OP76_0 combining another extended SC with over 26 h of RTP operations. The final day of lunar surface operations began with OP77_0, which ran for 2.75 h. LuGRE restarted during sunset operations with OP77_1 and ran just under 1.25 h past full sundown. LuGRE and Firefly coordinated a sequence of operations to be executed just before loss of power to the lander, which included switching to the

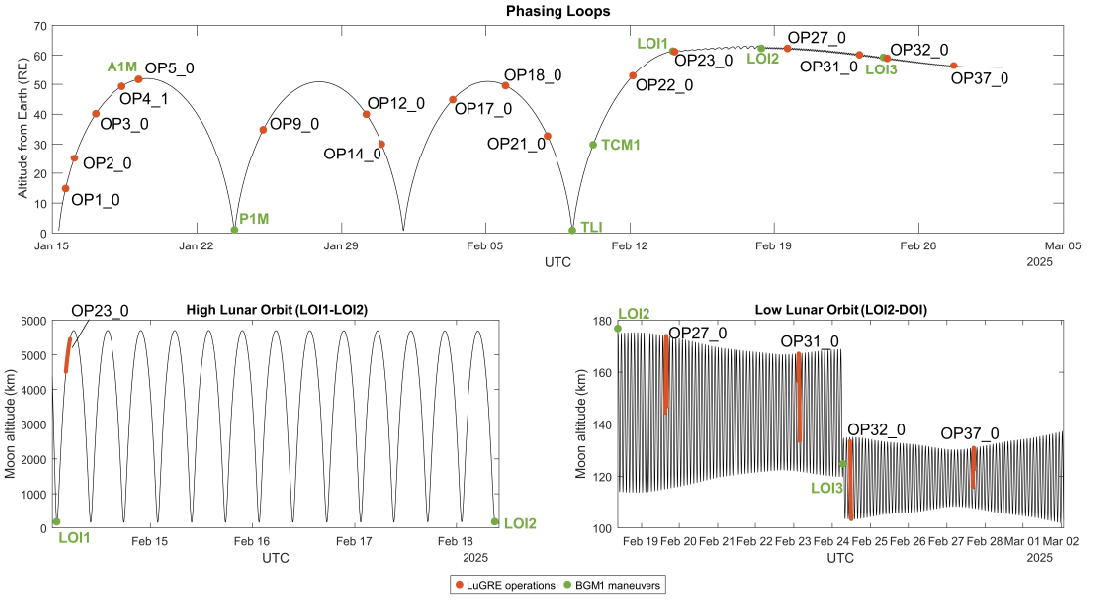

(a)

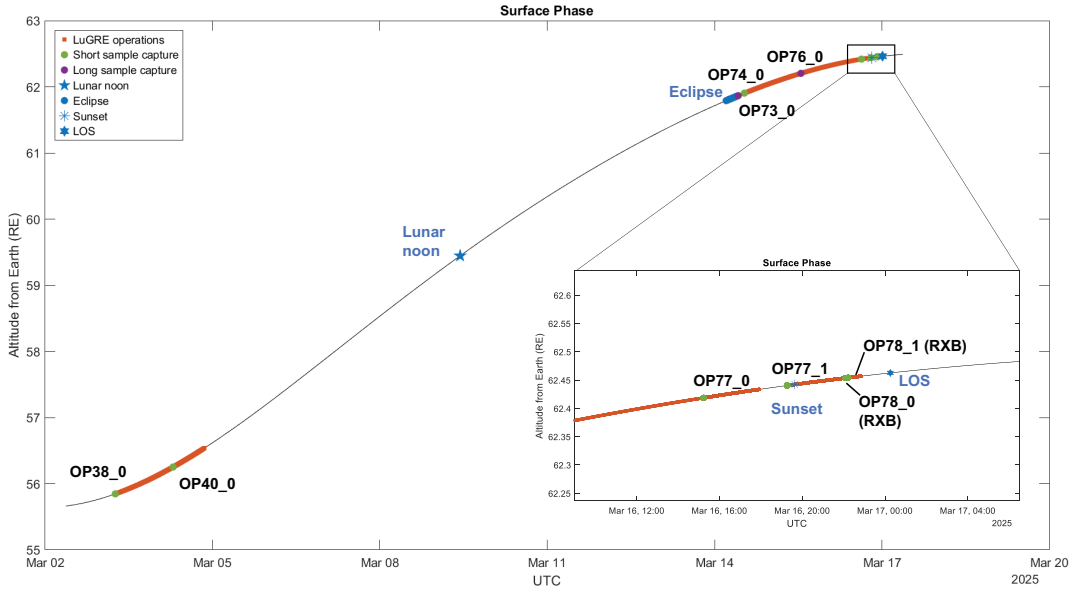

(b)

FIGURE 8 As-flown LuGRE operations. (a) As-flown transit operations, (b) As-flown surface operations.
Altitudes are referenced to the Earth geoid. DOI: descent orbit insertion; TCM: trajectory correction maneuver

second receiver (RXB), executing an I/Q SC, and then executing a full RTP operation on RXB until power was lost. LuGRE lost power on March 16 at 22:50 UTC, followed by the BGM1 lander's final loss of signal (LOS) at 23:15 UTC, ending the mission several hours into the lunar night, as planned.

Table 8 in Appendix A summarizes the LuGRE operations as executed, including the ID, receiver used, starting altitude, times and duration, and SC configuration.

Overall, LuGRE performed 16 discrete operations while in flight to the Moon, including 2 for commissioning, 9 scientific operations in the Earth-centered phasing loops, and 5 in lunar orbit. Overall, 14 of these operations returned IQSs, and 14 returned real-time measurements. LuGRE operated for a cumulative time of more than 111 h, collected approximately 12 s of IQS batches, and spent more than 106 h in RTP mode. The majority of LuGRE's operating time was on the lunar surface, where it successfully operated for over 95 h and collected 7 short-duration and 2 long-duration IQS batches, as shown in Table 8. Nearly 93 h were spent in RTP mode on the lunar surface, including over 3 h past the beginning of lunar sunset.

LuGRE set several records during its mission, including the following:

January 19 Successfully acquired and tracked signals from the GPS and Galileo constellations and, at 05:43:32 UTC, calculated a navigation fix at approximately 329,982 km from Earth's surface. The signals tracked during the fix time were GPS pseudorandom noise (PRN) 10 (L5), 21 (L1), and 31 (L1) and Galileo PRN 13 (E1 and E5a) and 15 (E5a).

February 14 Successfully acquired and tracked signals from the GPS and Galileo constellations in lunar orbit. The signals tracked were GPS PRN 1 (L1 and L5) and Galileo PRN 26 (E1 and E5a) and 33 (E1 and E5a). The maximum altitude at which a signal (Galileo PRN 33) was tracked was 390,416 km.

March 3 Successfully acquired and tracked signals from the GPS and Galileo constellations and, at 06:51:35 UTC, calculated the first GNSS-based navigation fix on the lunar surface, at a distance of approximately 356,237 km from Earth's surface. The signals tracked were GPS PRN 18 (L1 C/A and L5) and 25 (L1 C/A and L5) and Galileo PRN 2 (E1 Open Service [OS] and E5a) and 34 (E1 OS and E5a).

March 16 Successfully acquired and tracked signals and calculated a navigation fix at the most distant point, 398,350 km from Earth's surface. The signals were GPS PRN 12 (L1) and 25 (L1 and L5) and Galileo PRN 11 (E1 and E5a) and 24 (E1 and E5a). The receiver also tracked signals at nearly the same distance during the low lunar orbit phase, under orbital conditions. The longest-range signal tracked was Galileo PRN 11 at a distance of 433,220 km at 22:36:17 on March 16, 2025, on both E1 and E5a frequencies.

Figure 9 summarizes the total quantity of time during which each specific satellite was tracked by the LuGRE receiver, deriving measurements such as C/N_0, pseudorange, Doppler, etc. The PRNs listed in the figure but without any measurements—GPS 8, 9, 17, and 19, and Galileo 4, 6, 19, and 29—were only available at low C/N_0, likely corresponding to side-lobe signals, and were never successfully tracked.

4.1 | Characteristics of the Operational Environment Relevant to a GNSS User

Several properties of the environment in which LuGRE operated necessarily influenced either the receiver's ability to acquire and track signals or the characteristics of the resulting observables and state estimates. This section discusses two of the most influential factors: (1) the highly dynamic thermal environment associated with cislunar space and the lunar surface (a fact of physics) and (2) the capability of the lander to achieve precise Earth-pointing for signal reception (an operational service provided by a host vehicle). Both of these factors, being generally outside of

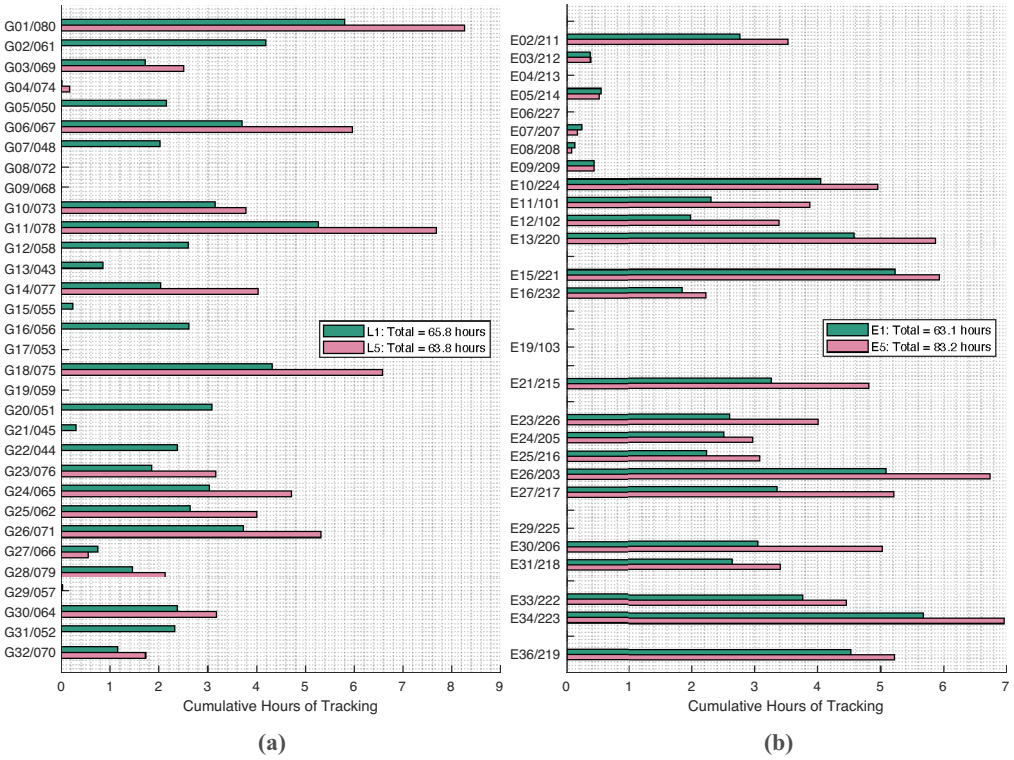

FIGURE 9 Cumulative number of hours of measurements collected for each GPS (G) and Galileo (E) satellite. (a) GPS L1 C/A/L5, (b) Galileo E1 OS/E5a.
Satellites are labeled by PRN and space vehicle ID (SVID), e.g., PRN/SVID. Inactive/unhealthy satellites were excluded; therefore, satellites with no data indicate no tracking at any point during the mission.

the direct control of the LuGRE team, may reasonably be expected to also impact most other lunar GNSS users and are therefore informative to highlight for contextualizing the data collected by LuGRE as well as for planning future missions.

4.1.1 | *Temperature*

The BGM1 mission experienced a wide range of thermal conditions, which are important to understand because of their impact on the LuGRE payload, especially the receiver clock. Figure 10 illustrates an example of the impact of fluctuating temperature on the clock drift estimated by the receiver during the first 24 h of surface operations. The strong correlation between the clock stability and the temperature experienced by the hardware is immediately clear.

Firefly placed three LuGRE-specific temperature sensors to monitor thermal conditions for payload safety. The sensors for the receiver and LNA were placed adjacent to these components, whereas the sensor for the HGA was placed on the back side of the antenna panel, centered on the HGA. Therefore, the values reported by these sensors, while not necessarily the precise absolute temperatures experienced by each component, offer a proxy for the relative levels and overall trends experienced by the hardware.

Figure 11 shows the three temperature profiles reported by these sensors during the transit phase. The temperature ranges of the receiver and LNA are similar owing to their common location within the upper chamber of the lander and were generally stable around the expected nominal temperature of 20 °C. The HGA was

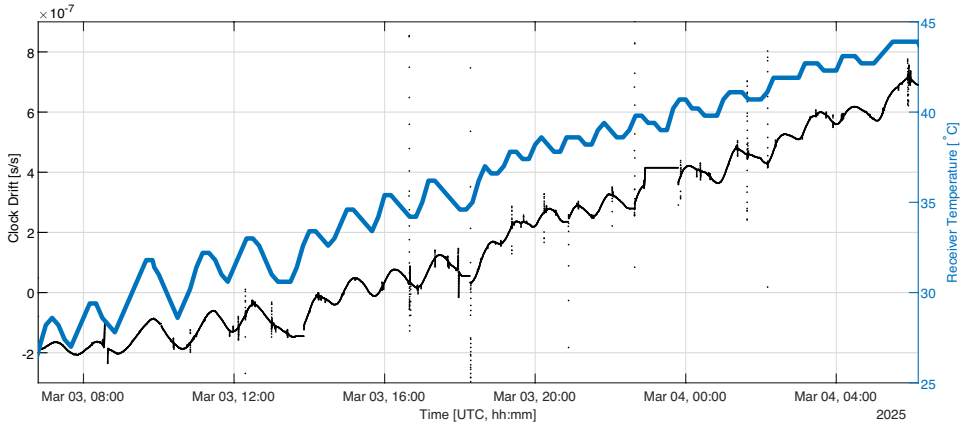

FIGURE 10 Receiver temperature and resulting clock drift behavior during early surface operations (as reported in the receiver POD telemetry)
The overall rising trend is due to increasing solar illumination, with smaller fluctuations due to the thermal output of other hardware components on the lander. It is clear that these thermal phenomena had direct impacts on the clock drift of the LuGRE receiver.

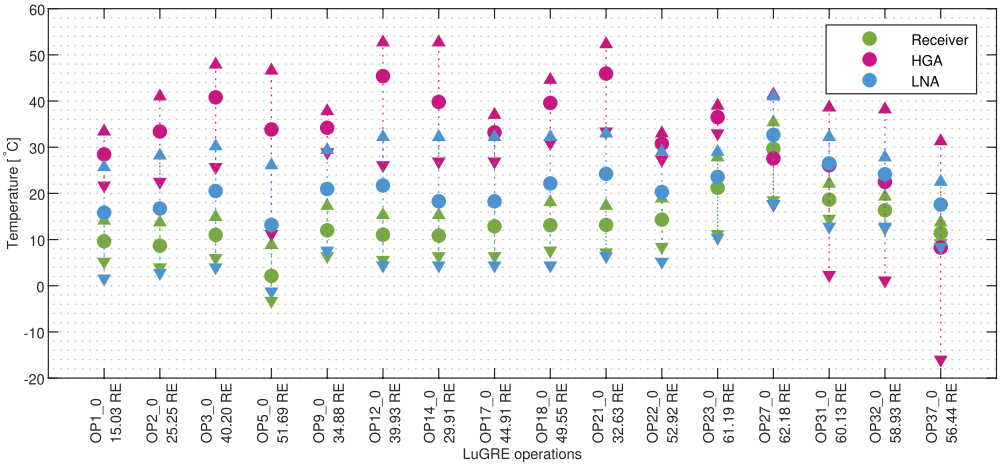

FIGURE 11 Temperatures observed during transit operations for the receiver, LNA, and HGA hardware
The mean value for each operation is depicted by a circle, with ranges above and below depicted by arrows.

typically hotter in the Earth-phasing loops and colder while in lunar orbit as compared with the receiver and LNA because of the radiative heating and cooling in its exposed position on the lander's pointing platform.

Figure 12 shows the temperature profiles reported by the same sensors during the surface phase. This phase was highly thermally dynamic, correlating closely with solar illumination as well as the thermal output of other components on the lander, particularly those closest to the LuGRE receiver and LNA. The temperature of all LuGRE components rose steadily throughout the first three days of surface operations until just before 00:00 UTC on March 5, at which point LuGRE was powered off during OP40_0. During the power-off period (not shown in this figure), temperatures continued to rise. The temperatures of the receiver and LNA were primarily influenced by the thermal output of other components of the lander, peaking at 72 °C on March 7 and 68 °C on March 6, respectively. The sun-exposed HGA was the hottest component by far, ultimately peaking at 115 °C on March 10.

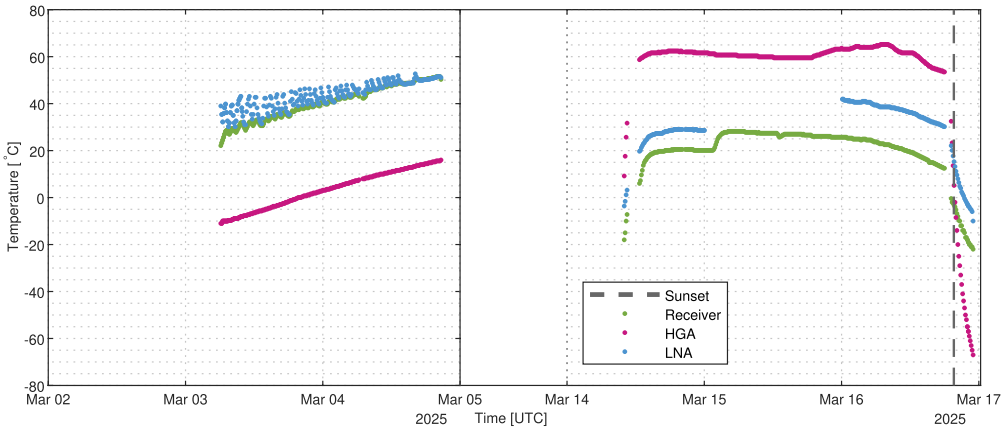

FIGURE 12 Temperatures observed during surface operations for the receiver, LNA, and HGA hardware
Temperatures during the power-off period between March 5 and March 14, 2025, are not shown.

Peak temperatures were all within yellow limits for the hardware, meaning that components were expected to survive with no significant damage as long as they remained powered off. During OP73_0, temperatures were briefly low, owing to the preceding eclipse, but quickly rose back to pre-eclipse levels, similar to those observed at the beginning of OP38_0, before declining steadily as the sun set. The final operations spanning lunar sunset on March 16 experienced a swift temperature decrease of 35 °C over a 5-h span for the internal components, with a greater decrease observed for the HGA.

4.1.2 | *Antenna Pointing*

Receive antennas for high-altitude GNSS users are typically designed with relatively high gain compared with terrestrial users, often resulting in consequently narrow gain patterns; for example, see the LuGRE HGA gain patterns in Figure 3. Because of this design type, small errors in pointing the receive antenna toward the Earth can result in increasingly large losses in the received C/N_0. LuGRE required that the BGM1 lander point the LuGRE HGA to within 1° of the Earth's center for the duration of all data collection to guarantee visibility of GNSS signals within the peak gain region of the HGA gain pattern without significant gain roll-off due to mis-pointing. This requirement was met for all operations, with a margin. The statistics of the actual achieved off-pointing error are shown in Figure 13. Off-pointing was calculated using the Firefly-provided definitive lander attitude for transit and antenna gimbal angles for the surface phase.

Throughout transit phase operations, an off-pointing angle of less than 0.73° from the Earth's center was achieved by the lander, with a median value of 0.35°. While on the lunar surface, the achieved off-pointing accuracy was better than 0.21° from the Earth's center, with a median value of 0.05°. The difference in accuracy between the phases is likely due to the methods used by the lander to obtain Earth-pointing attitude; because the antenna panel was stowed during transit, antenna pointing could only be achieved with a full vehicle re-orientation, as opposed to finer gimbal control while on the surface. As discussed in Section 5.1.2, the as-flown lander attitude was incorporated into signal visibility simulations so that the precise receive gain can be accounted for in the link model, considering any off-pointing.

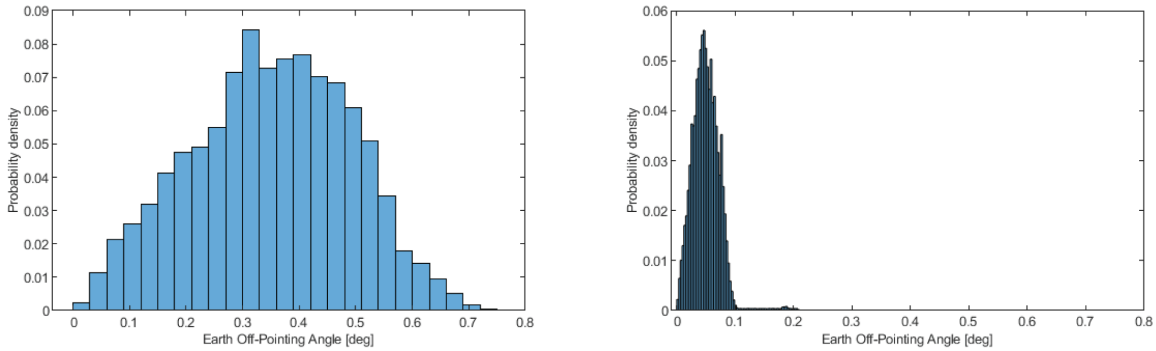

FIGURE 13 Achieved Earth-center off-pointing angle statistics during the transit and surface phases of the mission. (a) Transit off-pointing: Probability distribution, (b) Surface off-pointing: Probability distribution.

5 | RESULTS

This section describes the top-level results of the LuGRE mission in the categories of signal strength, measurement quality, signal availability, receiver state estimation, and IQS characterization. These categories represent the core investigations described in the LuGRE science plan (Konitzer et al., 2024) and therefore form the basis for extended results and analysis in future work.

5.1 | Received Signal Strength

The GNSS received signal strength was analyzed in terms of C/N_0 estimates collected at a rate of 1 Hz during RTP mode operations of the LuGRE payload. The C/N_0 values were estimated at the receiver tracking stage via pilot channels, i.e., GPS L1 C/A and L5Q and Galileo E1C and E5a-Q; therefore, this analysis reflects the signals that the LuGRE payload was actually capable of tracking during the assigned operations (Parker et al., 2022).

5.1.1 | Results and Characteristics

Aggregating the statistics of the observed C/N_0 as histograms of normalized C/N_0 occurrences enables a distinction between signal contributions originating from the antenna main- and side-lobes of the GNSS satellites. Unlike terrestrial observations, where only main-lobe signals are tracked, this representation provides key insights into the unique signal environment experienced by the LuGRE payload in cislunar space and on the lunar surface.

Representative results are shown in Figure 14 to familiarize the reader with the different tracking scenarios encountered throughout the mission. On the left side of each subfigure, a space skyplot characterizes the relative geometry between the spacecraft and the tracked GNSS satellites during the operation, assuming a nadir-pointing attitude (i.e., the LuGRE HGA is considered to be perfectly aligned with Earth's center). The center-of-mass positions and velocities of the GNSS satellites—originally broadcast in the constellation-specific Earth-fixed rotating frame—are transformed into the spacecraft's local-vertical, local-horizontal frame defined by the Firefly BGM1 definitive ephemerides, capturing their apparent

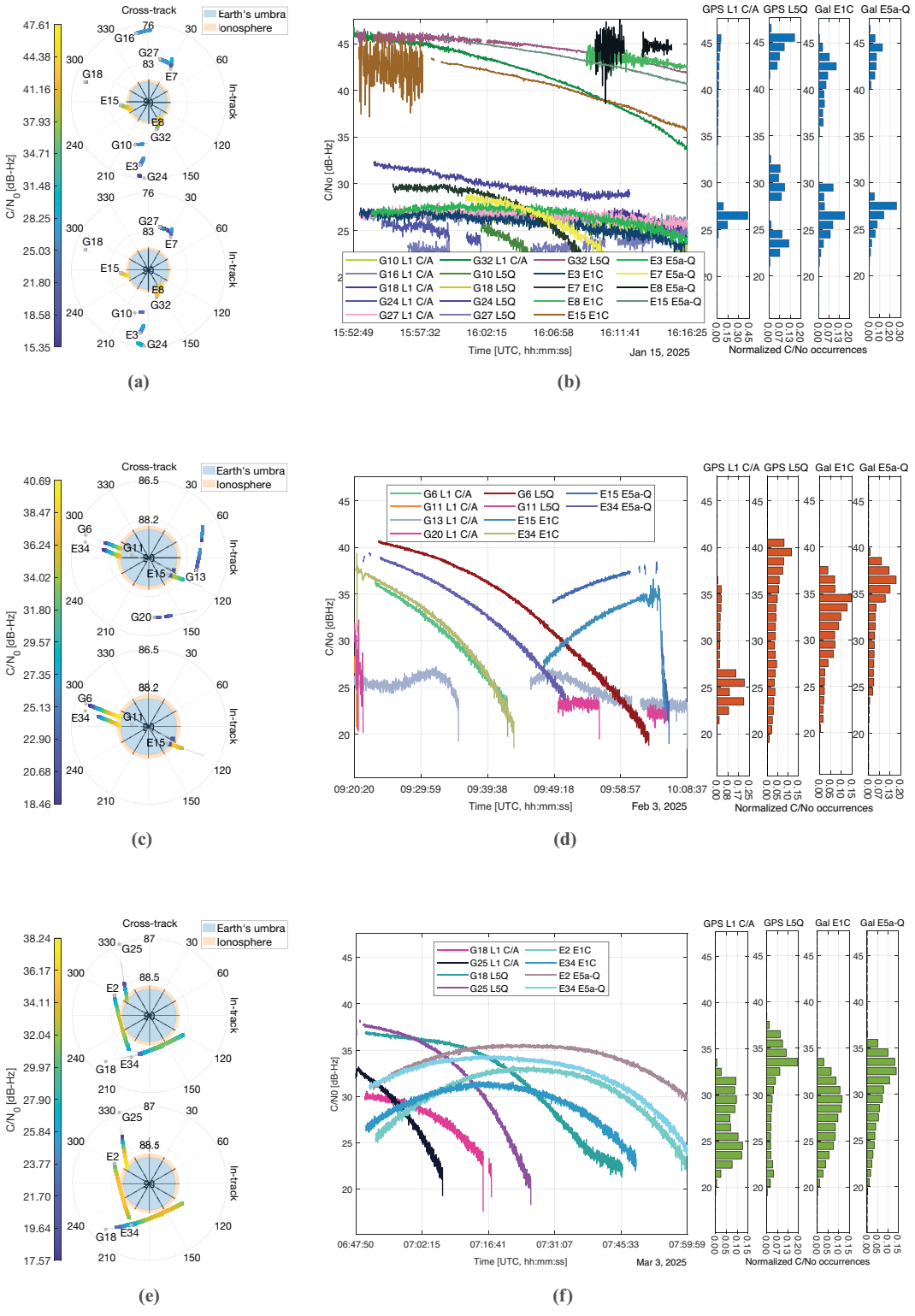

FIGURE 14 Space skyplots (left) and corresponding C/N_0 time series with normalized histograms (right) for three representative LuGRE operations from different mission phases. (a) OP1_0: Space skyplot; L1 C/A/E1C (top) and L5/E5a-Q (bottom). (b) OP1_0: C/N_0 time series and histogram for 15-RE altitude. The group of tracked signals below approximately 33 dB-Hz arises from transmitter side-lobes. (c) OP17_0: Space skyplot; L1 C/A/E1C (top) and L5/E5a-Q (bottom). (d) OP17_0: C/N_0 time series and histogram for 44.9-RE altitude. The group of tracked signals below approximately 27 dB-Hz are from transmitter side-lobes. (e) Extract of OP38_0 (initial 72 min): Space skyplot; L1 C/A/E1C (top) and L5/E5a-Q (bottom). (f) OP38_0 (initial 72 min): C/N_0 time series and histogram at the lunar surface (55.8-RE altitude). All tracked signals shown are from transmitter main-lobes.

Histograms are grouped by GNSS signal component. The C/N_0 time series legend refers to RINEX observation codes.

motion from the receiver's perspective. The Earth's disk and surrounding ionosphere layer are overlaid as a shaded region. Each satellite trajectory is plotted as a gray solid line, overlaid with a heatmap that encodes the C/N_0 values for each tracked signal component, separately for the L1/E1 (top diagram) and L5/E5a (bottom diagram) frequency bands. Such an augmented visualization allows for the identification of regions in which main-lobe and side-lobe tracking occurs. Stronger signals typically cluster near the Earth's limb, suggesting main-lobe reception, whereas weaker signals are observed at lower elevations, often associated with side-lobe contributions. To complement the geometric and time series perspectives, C/N_0 values are statistically aggregated from the time series and presented as histograms of normalized occurrences on the right side of each subfigure, providing a quantitative view of the signal strength distribution across the LuGRE receive bands.

The first effect observed in the time series of Figure 14(b) is the presence of specific satellite signal components whose C/N_0 estimates exhibit high variance, particularly at the beginning of their tracking window (e.g., PRN 15 on E1, PRN 8 on both E1 and E5a, PRN 32 on both L1 and L5). This behavior can be interpreted by jointly analyzing the corresponding skyplot in Figure 14(a), which shows that these fluctuations are associated with satellites whose trajectories graze the Earth's limb and intersect the ionospheric layer. In particular, these components are often observed in transition phases, where GNSS signals may still reach the receiver even when the direct path is geometrically obstructed, owing to refraction in the ionosphere. The oblique propagation path introduces additional ionospheric delay and potential phase distortion, while spatial inhomogeneities along the signal path give rise to scattering. These effects collectively contribute to increased variability in the estimated C/N_0 values due to unstable signal tracking.

Another key observation characterizing this low-altitude LuGRE operation (see Table 8) is the emergence of a threshold—at approximately 33 dB-Hz—that serves as a qualitative boundary between main-lobe and side-lobe tracking. This distinction is evident both in the skyplot, where side-lobe signals are predominantly concentrated at lower elevation angles, and in the multimodal C/N_0 distributions, which indicate that a substantial portion of the occurrences are below 33 dB-Hz.

In contrast, Figures 14(c) and 14(d) illustrate primarily main-lobe tracking. For example, both PRN 6 on L1/L5 and PRN 34 on E1/E5a are tracked down to the receiver's sensitivity threshold while remaining within the main-lobe regime. Conversely, PRN 15 on E1/E5a is initially tracked at low C/N_0, with the signal strength gradually increasing until signals become occluded by the Earth. On the other hand, PRNs 13 and 20 on L1 appear to be side-lobe receptions occurring above the receiver's sensitivity threshold, as also confirmed by the satellites' positions in the polar diagram.

Lastly, Figures 14(e) and 14(f), which correspond to the initial portion of the first surface operation, show a reduced number of tracked signals, all attributed to main-lobe reception. Among them, PRNs 2 and 34 on E1 are initially tracked closer to the receiver sensitivity limit—approximately 5 dB lower than their E5a counterparts—and their signal strength progressively increases as the satellite track moves toward the Earth's limb. Conversely, GPS channels start being tracked at higher C/N_0 and fade toward the sensitivity threshold as Earth's occultation occurs.

The trends shown in Figures 14(a)–14(f) are further confirmed by the statistical patterns in the corresponding C/N_0 histograms. High-intensity modes typically reflect strong main-lobe contributions (e.g., Figure 14(b)), whereas lower modes are associated with side-lobe reception (e.g., Figure 14(d)). In some cases, long tails extending from high or near-high modes indicate that main-lobe signals were

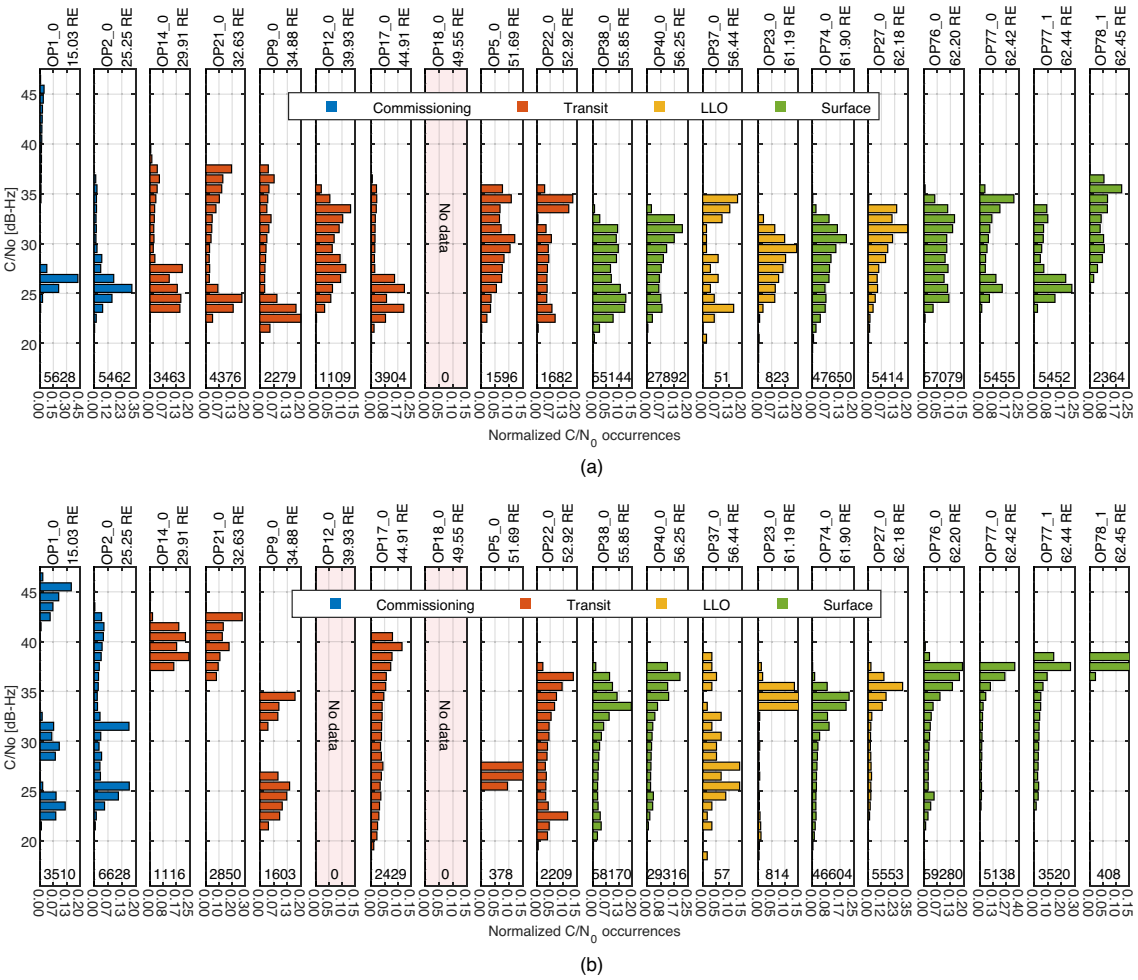

FIGURE 15 Normalized C/N_0 occurrences for GPS signals throughout mission operations. (a) GPS L1 C/A, (b) GPS L5Q.
Operation IDs and associated altitudes are reported at the top of each histogram. The total number of C/N_0 estimates is reported at the bottom of each subplot. Operations are sorted from lowest altitude on the left to highest on the right.

tracked down to the receiver's sensitivity threshold (e.g., Figure 14(f)), whereas side-lobe signals more often fall below trackable levels.

Figures 15 and 16 show the normalized occurrences of the C/N_0 estimates throughout all transit and surface operations for GPS and Galileo signals, respectively. The histograms, sorted by initial operation altitude, present the normalized distribution of C/N_0 estimates obtained during each operation and collected by 2-dB bins in the interval of 18–48 dB-Hz. The y-axis indicates the C/N_0 dynamic range whereas the x-axis shows the percentage of occurrences included in each bin. As the number of C/N_0 estimates differs for each operation, the representativeness of the corresponding histograms also varies. For this reason, the total number of estimates is reported at the bottom of each histogram as an indicator of statistical reliability. Different colors are used to distinguish mission phases.

As shown in Figures 15 and 16, the altitude and, consequently, the increase in free space path loss produce a decreasing C/N_0 trend and a reduction in the number of visible side-lobes. Note that the observed variability of C/N_0 ranges depends not only on altitude but also on mission phase. For instance, although OP27_0 is performed at a similar altitude as OP78_1, the visibility conditions and

dynamics during the low lunar orbit (LLO) phase yielded different behavior in the C/N_0 distribution.

5.1.2 | *Analysis of C/N_0 Levels*

The C/N_0 results shown in Figures 15 and 16 are significantly lower than the levels predicted both by the LuGRE GEONS planning simulation (see Section 3.2) and in the literature for systems with similar properties (see, e.g., the work by Hassouneh et al. (2023)). See Figure 17 for an example of the discrepancy observed during a lunar surface operation. To quantify and characterize this result, the LuGRE team further developed its planning simulation into an analysis tool. This section details the configuration and resulting C/N_0 discrepancy characterization.

GEONS and its GGMS front-end simulate C/N_0 using the model described in Section 12.5.4 of the GEONS Mathematical Specification (Long & Stacey, 2025). The inputs to this model in the simulations implemented by the LuGRE team are described in Table 3; link budget parameters specific to the LuGRE payload are shown in Table 4. Any additional terms or inaccuracies in the values shown in these

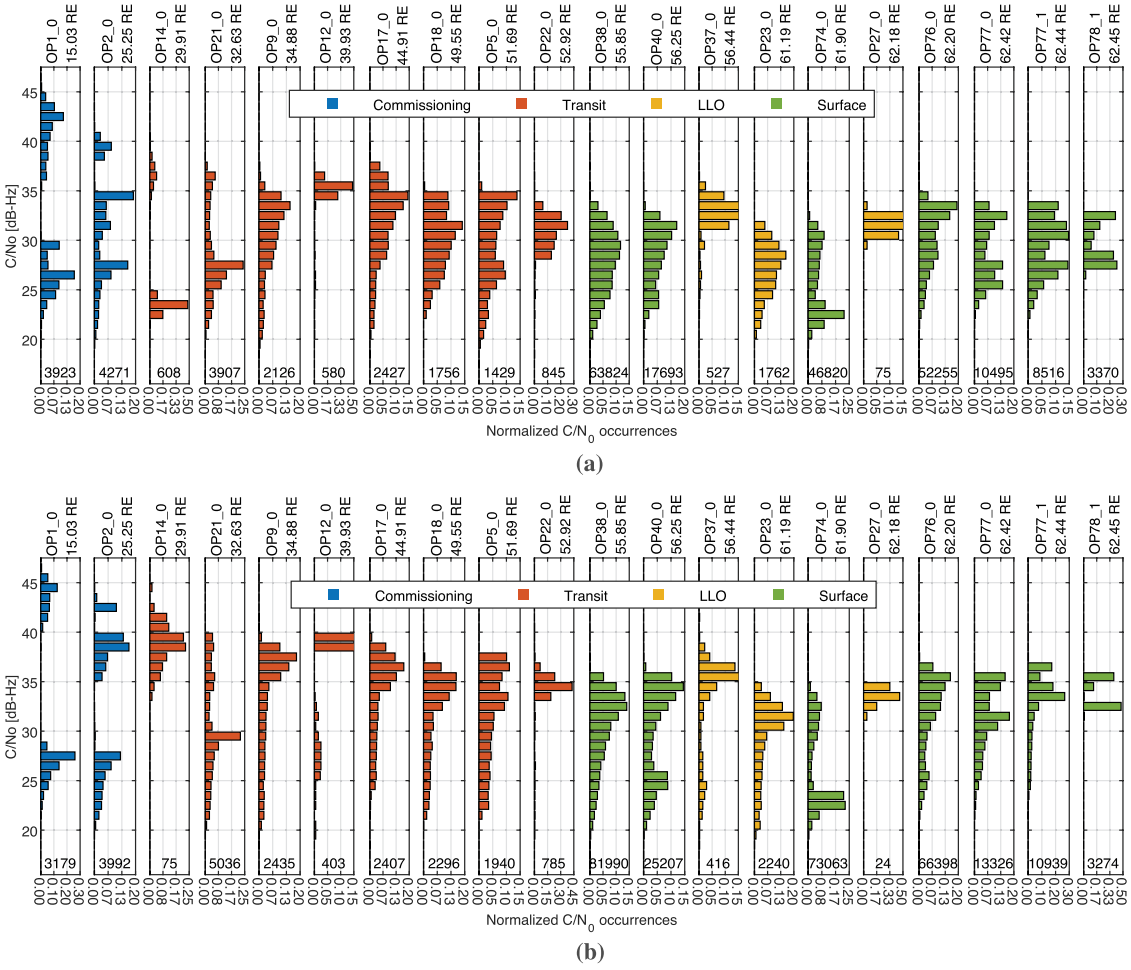

FIGURE 16 Normalized C/N_0 occurrences for Galileo signals throughout mission operations. (a) Galileo E1C, (b) Galileo E5a-Q.
Operations IDs and associated altitudes are reported at the top of each histogram. The total number of C/N_0 estimates are reported at the bottom of each subplot. Operations are sorted from lowest altitude on the left to highest on the right.

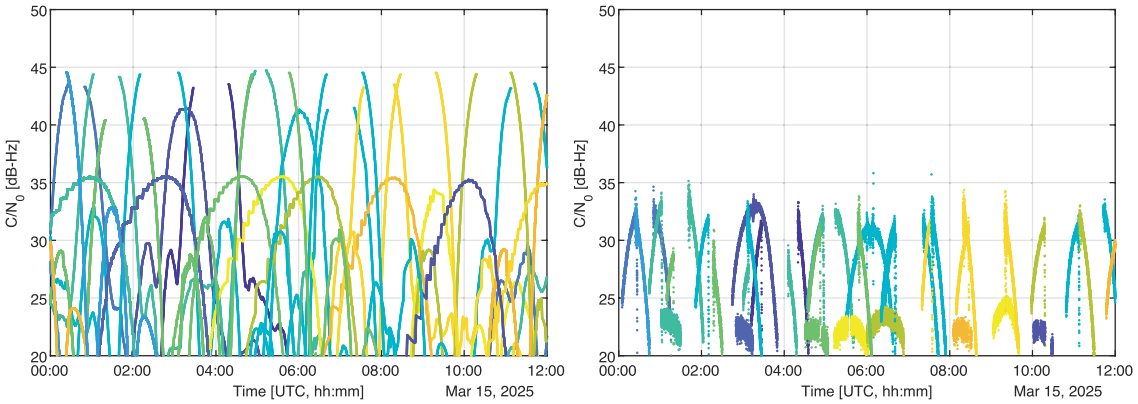

FIGURE 17 Example of C/A C/N_0 comparison between (a) simulation and (b) LuGRE flight data (lunar surface case)
Colors distinguish between different PRNs belonging to GPS blocks IIR-M and IIIA.

TABLE 3
C/N_0 Simulation Parameters

Parameter	Description
BGM1 trajectory[a]	Definitive lander ephemerides from post-processed orbit determination by Firefly; covariance within 100-m 1σ.
LuGRE antenna pointing[a]	Definitive lander attitude quaternions (in transit) and antenna-pointing platform gimbal angles (on surface) from Firefly. See Figure 13.
LuGRE antenna gain patterns[a]	Gain patterns measured by LuGRE in NASA GSFC anechoic chamber. Consistent with manufacturer-delivered pattern shown in Figure 3.
LuGRE link parameters[a]	Measured and estimated loss and noise parameters. See Table 4.
Transmitter position	Definitive constellation broadcast ephemeris (CDDIS daily files) for the time period spanning each LuGRE operation.
Transmitter attitude	Described in GEONS Mathematical Specification (Long & Stacey, 2025).
Transmitter antenna gain patterns	Published GPS IIR-M and IIIA L1 manufacturer patterns (NAVCEN, 2025).
Transmitter power	Per-satellite values; average of 16.5 dB (GPS IIR-M), 15.6 dB (GPS IIIA).

[a] LuGRE-specific parameter

tables, causing either lower-than-expected power (i.e., C) or higher-than-expected noise (i.e., N_0), are unknown to the simulation and are therefore contained in the C/N_0 discrepancy observed in-flight.

For the specific purpose of simulating C/N_0 to quantify the observed in-flight discrepancy, the analysis focused on only GPS L1 signals from blocks IIR-M and IIIA, as these blocks have well-documented transmit antenna gain patterns and transmit powers that can be validated using multiple sources. The relevant transmit antenna gain patterns are publicly available. The transmit power was estimated using public products from the Cyclone Global Navigation Satellite System (CYGNSS) mission over the timespan of the LuGRE flight data (CYGNSS, 2024). CYGNSS data provide

TABLE 4
LuGRE Link Budget Parameters

Parameter	Symbol	L1 C/A, E1 OS	L5, E5a	Source
System noise temperature	T_s	182K (22.6 dB)	231K (23.6 dB)	Cascade of RF hardware described in Section 3, using measurements of individual component properties
Receive antenna gain peak	G_r	15.35 dB	14.56 dB	Includes polarization and mismatch losses in the measured patterns shown in Section 3
Implementation loss	A_s	0[a] dB	0[a] dB	N/A

[a] The LuGRE flight payload implementation loss was not fully calibrated; therefore, the indicated value was used for all simulations.

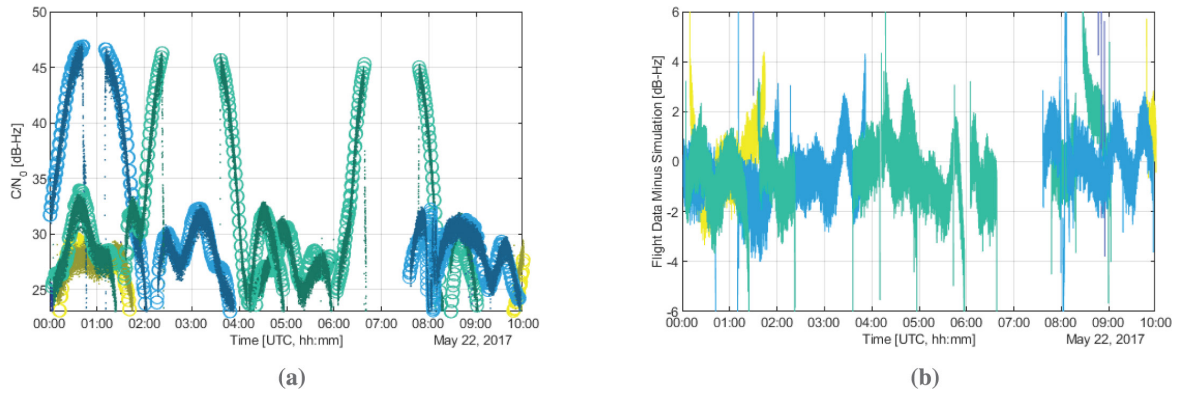

(a) (b)

FIGURE 18 Comparison between GGMS simulation results and MMS flight data. (a) Direct C/N_0 arc comparison between MMS flight data (dots) and simulation (circles), (b) $\Delta C/N_0$ (MMS flight minus simulation).
The focus is on GPS L1 C/A signals from block IIR-M. Colors distinguish between different PRNs belonging to the considered block.

the measured effective isotropic radiated power (EIRP), from which the transmit power can be derived by removing the transmit antenna gain at the elevation angle of the measurement (Wang et al., 2019). These values have also been corroborated within 0.5 dB by work analyzing the total received EIRP measured by ground receivers (Steigenberger et al., 2024; Steigenberger et al., 2018).

The validity of the simulation was evaluated by using it to simulate C/N_0 as observed by the MMS. By applying MMS link budget parameters (Winternitz et al., 2019) and comparing the results to MMS C/N_0 flight data over a period in 2017 at an altitude of 12 RE, we obtained the comparison shown in Figure 18 (Winternitz et al., 2017). The results are highly consistent, with an overall difference that is zero-mean with variation on the order of 1–2 dB, validating the configuration of the underlying models.

The validated simulation was then used to predict the LuGRE C/N_0, focusing on the well-known GPS L1 signal from block IIR-M and block IIIA satellites. Comparing LuGRE flight data against this simulation shows that the C/N_0 estimated in-flight is generally 7–12 dB lower than expected. Furthermore, this discrepancy is present across the full LuGRE data set, including at lower altitudes covered by the MMS validation data, and does not appear to correlate with external

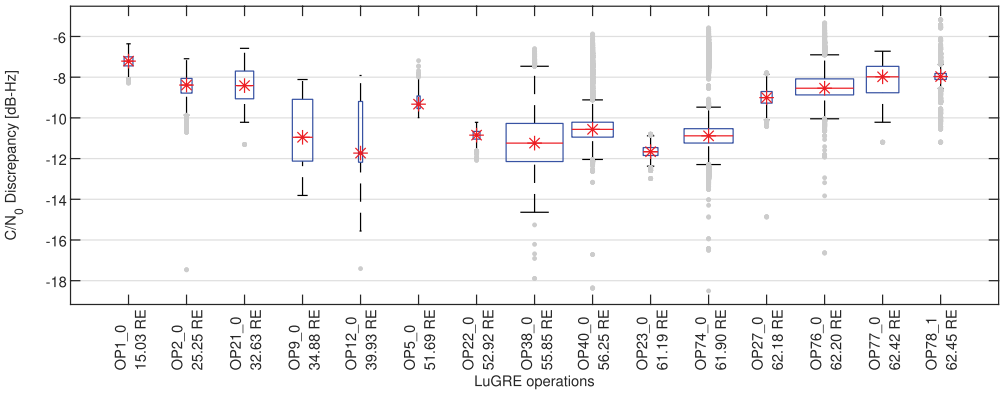

FIGURE 19 C/N_0 difference from simulation (dB, flight minus simulation) for GPS L1 blocks IIR-M and IIIA, summarized by operation
Operations are sorted from lowest altitude on the left to highest on the right; see Table 8 for details. Operations numbered OP38_0 and higher are surface operations. The plot is defined as in the MATLAB boxplot function. The box width is proportional to the square root of the number of data points used.

factors such as temperature, altitude, or mission phase (i.e., transit or surface; see Figure 19).

The root causes of this discrepancy are under investigation. However, the lack of clear correlation to a coincident property such as altitude or temperature and the fact that the discrepancy is not present in the MMS data at a similar altitude suggest causes within the overall integrated lander/payload flight system, not systemic transmission or environmental factors. In other words, the lower-than-expected C/N_0 observed by LuGRE is a peculiarity of this mission and should not be interpreted as an inherent characteristic of lunar-vicinity GNSS reception in general.

It is important to note that the in-flight results described elsewhere in this section are necessarily influenced by the observed C/N_0 discrepancy. The most obvious effect is on signal availability, as the overall lower C/N_0 level results in the majority of the GNSS side-lobe signals falling below the receiver acquisition threshold, as shown in Figure 17. Prior work has consistently shown that side-lobes are expected to be abundant at C/N_0 levels that can be reliably acquired and tracked at lunar distance (Ashman et al., 2024; Delépaut et al., 2020). Likewise, the properties of the GNSS observables are subject to thermal noise theory, such that the pseudorange, Doppler shift, and carrier-phase measurements collected by LuGRE inevitably have additional noise beyond what would otherwise be expected at higher C/N_0 levels (Kaplan & Hegarty, 2017).

5.2 | Measurement Quality

To assess the quality of the raw GNSS measurements collected during LuGRE, the standard deviation of the pseudorange ($\hat{\sigma}_\tau$) and carrier-phase ($\hat{\sigma}_\phi$) observables were computed by detrending the data using third-order finite differences with fourth-order accuracy. This approach allowed for the isolation of short-term fluctuations that are primarily attributable to receiver noise without long-term variations induced by the dynamics of the scenario, enabling a direct assessment of the intrinsic precision of the measurements for the different signal components across the mission phases.

Note that during a single operational window, the same signal component can be acquired and tracked multiple times with different quality levels owing

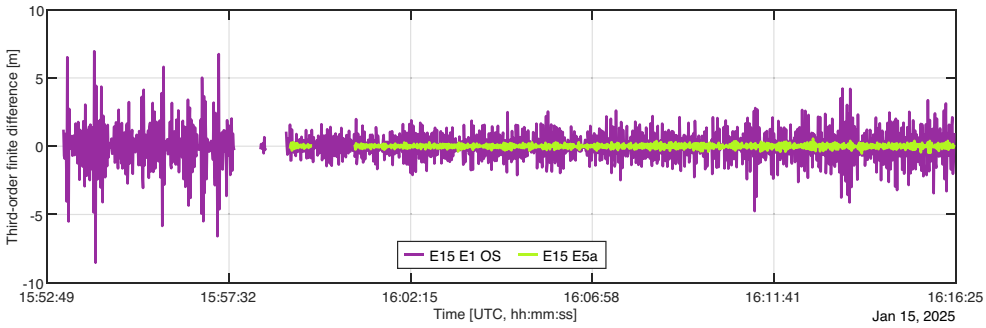

FIGURE 20 Examples of third-order finite difference of code pseudorange measurements from OP1_0

to potentially different propagation conditions, especially for satellites tracked right before being occluded by the Earth or just rising from an occlusion window, compared with time intervals during which they are in full visibility. For example, Figure 20 shows the behavior of the third-order finite difference computed over the time series of code pseudorange measurements for Galileo PRN 15 (E15 E1 OS) in two distinct timespans, characterized by different standard deviations. The code measurements were not corrected for the estimated receiver clock bias before computation of the finite differences. Additionally, the C/N_0 value may vary during each operational window, as highlighted in Figure 14(b). For these reasons, the detrended time series for each satellite signal component (i.e., for each active receiver channel) was analyzed by identifying multiple continuous, uninterrupted intervals of tracking for that channel. To account for this variability, the standard deviation was estimated separately for each tracking interval and then combined using a weighted average, with weights equal to the ratio between the number of samples in each partial interval and the total number of non-null samples of the time series. For each LuGRE operation, this methodology yields a unique value per satellite signal component. Although this method enables comparability across channels, the statistical precision may vary, as channels tracked more extensively and under more stable conditions are statistically more significant.

Figure 21 presents the estimated standard deviation of code pseudorange (Figure 21(a)) and carrier-phase (Figure 21(b)) measurements across LuGRE operations, grouped by GNSS signal type (i.e., GPS L1 C/A, GPS L5, Galileo E1 OS, Galileo E5a). The analysis spans all mission phases, from flight to surface operations (see Table 8), with results sorted by their initial altitude. The standard deviation is calculated over the full operation span for each tracked satellite, and correlation to C/N_0 or other factors is left for future work.

The results show good quality of the receiver measurements in all mission phases, comparable to what is typically achieved on Earth for the considered front-end bandwidth (Ribot et al., 2016). As expected, code measurements exhibit estimated standard deviations approximately two orders of magnitude higher than those of carrier-phase measurements, consistently reflecting the well-known difference in precision between code and phase tracking. Beyond this general trend, the results highlight meaningful differences across frequency bands and signal modulations. In particular, channels in the L5/E5a band consistently show lower code measurement noise than their L1/E1 counterparts. This behavior is due to a combination of factors: wider signal bandwidth, lower path loss, and higher EIRP such as in the case of Galileo E5a compared with E1 OS (Menzione et al., 2024). These characteristics typically result in higher observed C/N_0 levels (see Figure 16), improving the stability of code tracking loops and reducing thermal-noise-induced jitter, which

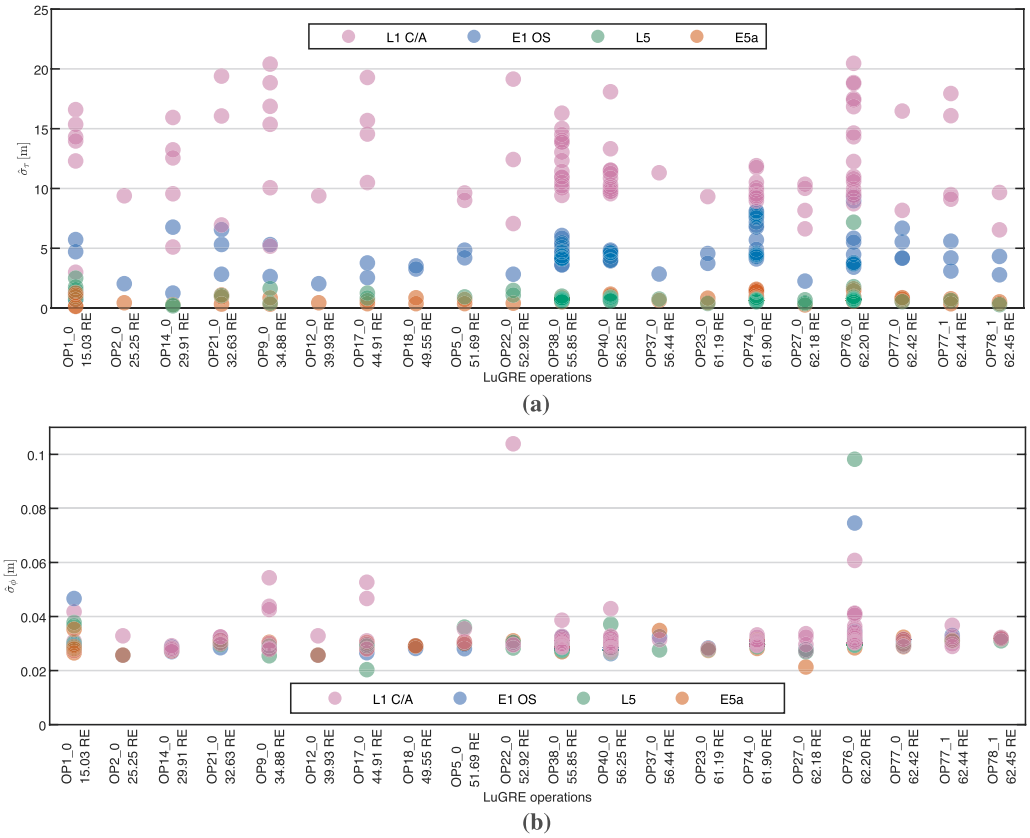

FIGURE 21 Estimated standard deviation of GNSS code and carrier-phase measurement noise across LuGRE operations, grouped by signal component. (a) Code measurements, (b) Carrier-phase measurements.
Each marker corresponds to a tracked signal component from a specific satellite. Operations are ordered according to the spacecraft's altitude at the start of each operation. Operations are sorted from lowest altitude on the left to highest on the right.

represents the dominant source of residual noise on code measurements (Won & Pany, 2017). Even within the same bandwidth, differences are visible. For example, Galileo E1 OS observables exhibit lower noise than GPS L1 C/A, potentially because of the composite binary offset carrier modulation, which theoretically offers better performance. This modulation narrows the main-lobe of the autocorrelation function and improves the sensitivity of the code discriminator to small timing errors (i.e., a steeper discriminator slope around the prompt correlation), thus improving the receiver's ability to suppress thermal-noise-induced jitter in the code tracking loop (Betz, 2015; Betz & Kolodziejski, 2000).

In contrast, carrier-phase measurements show less overall variation across signal modulations. Because the precision of phase tracking is also influenced by the signal wavelength, L5/E5a signals—despite their favorable C/N_0—do not always yield reduced noise variance compared with their higher-frequency counterparts. Although most satellite signal components fall within a consistent range of estimated standard deviation values, a few outliers are clearly visible in specific operations. These outliers are the result of signal degradations not yet sufficient to trigger a loss of lock but capable of impairing the loop stability. These degradations have a significant impact on the statistics owing to the short durations of such tracking intervals. In general, these results, including the relative behavior of different modulations, align well with theoretical expectations based on the Cramér–Rao

bound for the maximum likelihood estimation of code delay and carrier-phase offset (Das et al., 2020; Medina et al., 2020).

5.3 | Signal Availability

Signal availability in a GNSS generally refers to whether the GNSS signals of interest are present, trackable, and usable at a given receiver location and time (Betz, 2015). Signal availability is impacted by geometric and radiometric visibility, which, in turn, depends on receiver sensitivity. The following analysis additionally applies a further condition: that the GNSS signals are strong enough to be acquired and tracked above the receiver's minimum C/N_0 threshold.

PVT availability extends beyond just having signals and is more restrictive, referring to whether the available signals and associated measurements (pseudorange, carrier phase, Doppler shift, etc.) are sufficient to solve for a multilateration solution with no *a priori* information of the receiver state (Kaplan & Hegarty, 2017). Thus, PVT availability is highly dependent on the specific time frame at which the operation took place, and even operations at similar altitudes can have different relative PVT availabilities. The following analysis provides an indication of both signal and PVT availability by counting distinct satellite signals at each epoch in RTP mode.

Figure 22 shows bar charts depicting overall GNSS signal availability throughout transit and surface operations, sorted according to the initial altitude of each operation. Each bar corresponds to an RTP operation and is color-segmented to represent the percentage of time, relative to the nominal duration of each RTP operation, during which exactly n signals from as many distinct n GNSS satellites were simultaneously tracked. To highlight PVT availability, cool-toned colors denote periods with $n \geq 4$ distinct tracked signals, indicating sufficient signal availability to compute a PVT fix through a well-determined least-squares algorithm, while warm tones highlight degraded visibility conditions ($n < 4$), where standalone positioning would not be feasible unless underdetermined multilateration problems are addressed leveraging some *a priori* knowledge about the receiver state (Vouch et al., 2025).

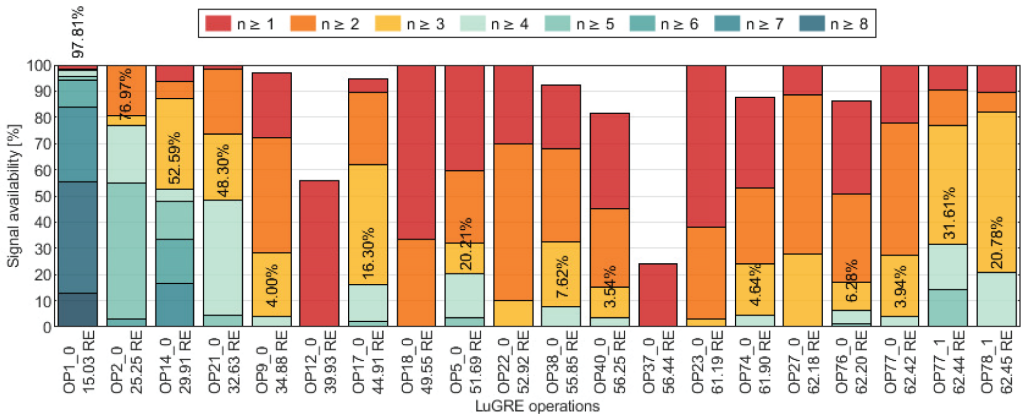

FIGURE 22 Multi-constellation, multi-frequency availability: Percentage of time, relative to the nominal duration of each RTP operation, during which n signals from as many distinct GNSS satellites were simultaneously tracked
Results are shown as a function of operation ID and associated altitude in RE. Percentage values are reported for $n \geq 4$.

A higher saturation of cool colors in a bar, such as in the case of OP1_0 and OP2_0, represents abundant signal availability throughout the operations. A few operations such as OP12_0 and OP37_0 were instead impacted by scarce signal availability due to poor geometric visibility of satellites.

The overall availability throughout the mission displayed in Figure 22 illustrates all tracked signals, for each frequency and constellation, reflecting the receiver's full tracking capability during the mission, with only one signal per satellite vehicle considered. Data have also been aggregated by constellation, as shown in Figure 23, where Figure 23(a) details GPS-only signals (L1/CA and L5 in-phase) and Figure 23(b) presents Galileo-only signals (E1 and E5a). A comparison of these results against Figure 22 clearly shows the expected benefit of using a multi-constellation receiver; this analysis shows how a single-constellation receiver would have limited opportunities to achieve a PVT fix, even during operations relatively closer to the Earth. Despite tracking multiple frequencies within each constellation, the number of unique satellites is limited by geometry, thus reducing overall availability.

Results are also shown by frequency band in Figure 24, where Figures 24(a) and 24(b) report signal availability over the L1/E1 and L5/E5a bands, respectively, aggregating the GPS and Galileo satellites. Table 5 summarizes the benefit of leveraging a multi-frequency receiver in the LuGRE mission by comparing the availability achievable using the L1/E1 signals only of Figure 24(a), compared with the full operational configuration illustrated in Figure 22. Although adding the second frequency does not change the geometry of the problem or the number of independent signals, the higher L5/E5a power and the wider beam of the transmit antenna

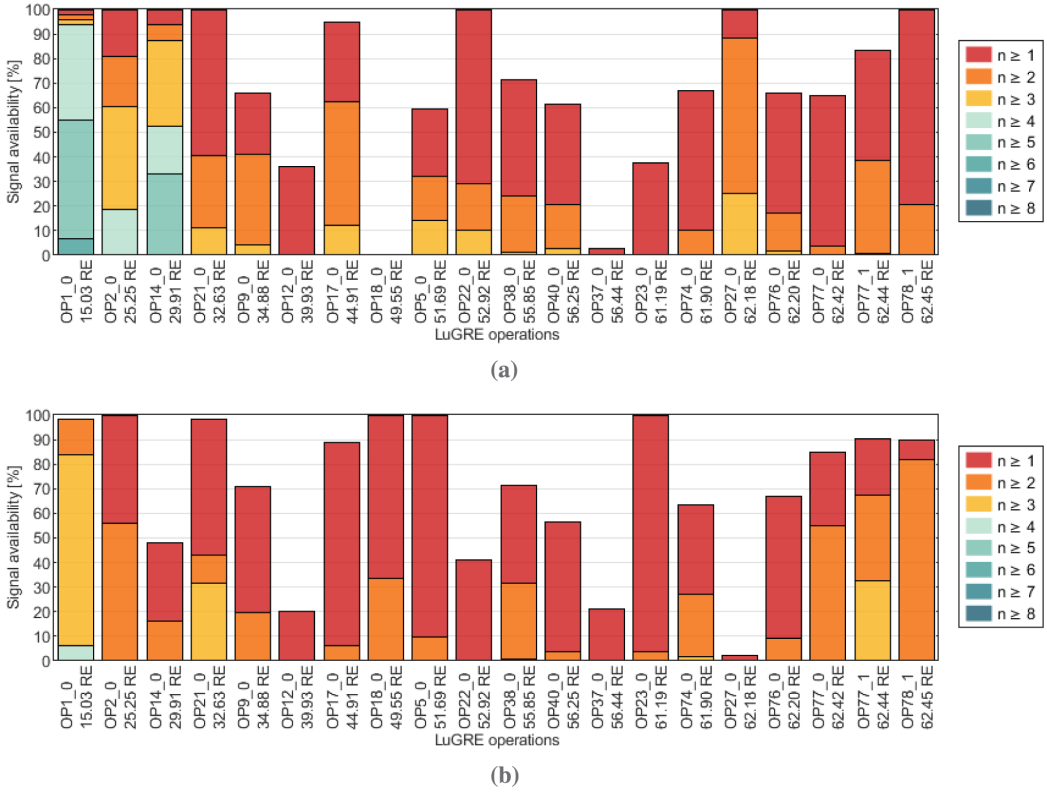

(a)

(b)

FIGURE 23 Single-constellation, multi-frequency availability: Percentage of time, relative to the nominal duration of each RTP operation, during which n signals from as many distinct GNSS satellites were simultaneously tracked. (a) GPS L1+L5, (b) Galileo E1+E5a. Results are shown as a function of operation ID and associated altitude in RE.

TABLE 5
Improvement in PVT Availability (i.e., $n \geq 4$) Achieved by Combining Multi-Frequency Observations, Compared with L1/E1-Only Processing

Metric / OP ID	1_0	2_0	14.0	21_0	12_0	17.0	5.0	23_0	74_0	27.0	76_0	77_0	77_1	78_1
L1/E1 avail. (%)	97.81	61.35	0.00	3.70	52.59	0.00	13.10	1.44	1.43	1.43	0.87	3.00	4.09	20.48
L1/E1+L5/E5a avail. (%)	97.81	76.97	20.21	4.00	52.59	16.30	48.30	7.62	3.54	4.64	5.94	3.94	31.61	20.78
Improvement (%)	0.00	15.62	20.21	0.30	0.00	16.30	35.20	6.18	2.11	3.21	5.07	0.94	27.52	0.30

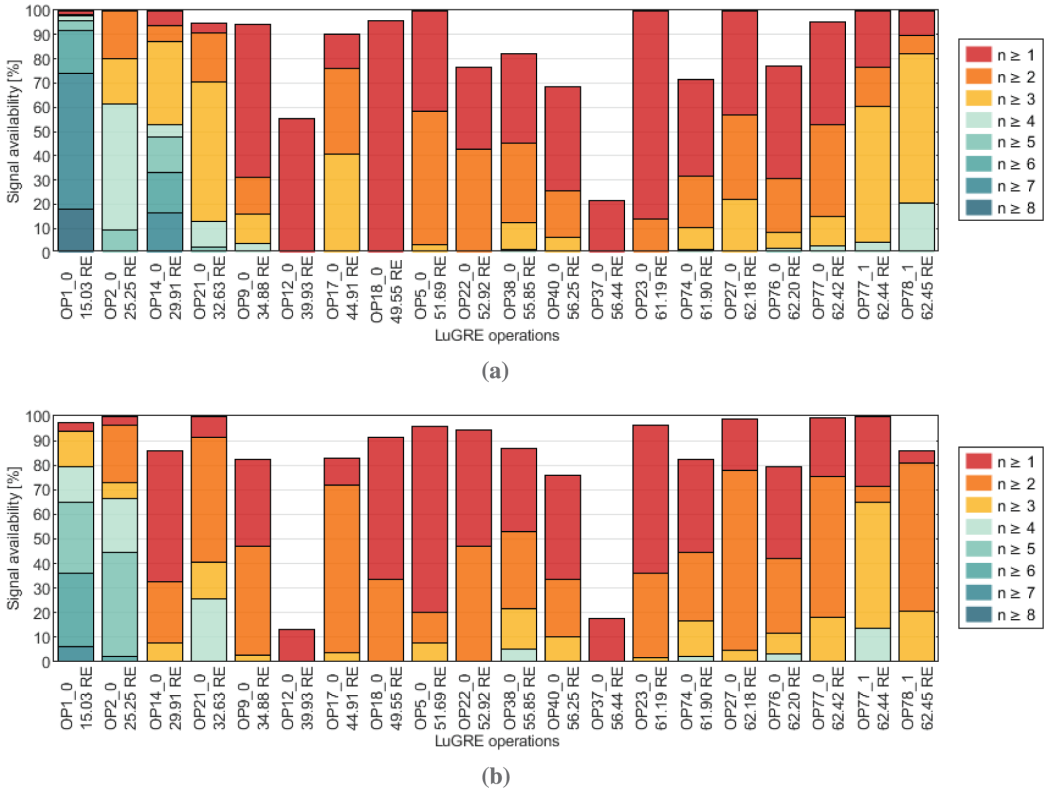

FIGURE 24 Multi-constellation, single-frequency availability: Percentage of time, relative to the nominal duration of each RTP operation, during which n signals from as many distinct GNSS satellites were simultaneously tracked. (a) GPS/Galileo L1/E1, (b) GPS/Galileo L5/E5a. Results are shown as a function of operation ID and associated altitude and associated altitude in RE.

pattern (Anthony, 2022a, 2022b; European Union, 2023; Menzione et al., 2024) increase the availability of signals. This trend is also reflected in the cumulative amount of data collected for each frequency, as shown in Figure 9.

5.4 | Receiver State Estimation

The LuGRE receiver featured both a POD extended Kalman filter and a weighted least-squares PVT algorithm for navigation, as described in Section 3.1. This section focuses on the PVT solutions; the characteristics of these results are less implementation-specific than sequential navigation filter solutions and thus extend more generally to future lunar users. Navigation filter analysis is left for future work. The LuGRE receiver produced instantaneous real-time PVT solutions during periods in which simultaneous visibility of signals was achieved for four or

more unique satellites. Overall, LuGRE calculated PVT solutions in both the transit and surface phases of the mission at altitudes ranging from 15 RE to 62 RE from the Earth's surface.

Table 9 in Appendix A provides a catalog of PVT windows throughout the LuGRE data set. Each row represents a contiguous time window in which a PVT solution was calculated by the receiver for a total time period comprised of at least 30 individual epochs without any gaps greater than 30 continuous seconds. The column denoted as "% NAV" refers to the percentage of time within each window in which a navigation solution was obtained by the onboard receiver, accounting for brief periods in which visibility falls below four unique satellites.

In nearly all cases, PVT solutions were achieved via a combination of constellations and frequencies. The column in Table 9 denoted as "% Multi-Const." refers to the percentage of time within each window in which at least one satellite from both GPS and Galileo was visible. In these cases, PVT availability was enabled by the GPS–Galileo time offset provided in the Galileo navigation message. Moreover, the overall signal availability was also impacted by the presence of the C/N_0 discrepancy discussed in Section 5.1.2; simulations suggest that without this discrepancy, the PVT availability would be greater.

As in any weak-signal GNSS application, the accuracy of PVT solutions is limited by the constellation/receiver geometry, as represented by the dilution of precision (DOP); Table 9 characterizes this specifically through the geometric DOP (GDOP). Over the LuGRE mission, the GDOP varied from a minimum below 50 in the lowest-altitude operation, to values averaging from 1,000 to 1,000,000 on the lunar surface, depending on the specific geometry.

Figures 25 and 26 show example error statistics from specific PVT windows, computed relative to the Firefly definitive trajectory characterized as in Table 3. Under poor geometric conditions, it is instructive to examine the range errors and root sum squared (RSS) lateral errors separately, as the range error becomes highly correlated with clock error and dominates the total solution accuracy at high altitudes (Konitzer et al., 2022).

OP1_0 at 15-RE altitude, shown in Figure 25, is the most comparable to typical GNSS use, although the GDOP is at a steady-state value of approximately 50. Here, the PVT error is generally between 100 m and 1 km in the range component and just over 1 km in the lateral component. Similarly, the velocity is under 10 m/s in both the range and lateral directions.

Figure 26 shows lunar surface PVT errors from OP38_0 during two representative time windows with different GDOP environments. The window with PVT error in blue shows a more dramatic variation around an asymptotic discontinuity in the GDOP. Here, the range errors are 1–100 km in position, and the velocity error is especially high, on the order of 1000–10,000 m/s. Lateral errors are more controlled, under 1 km in position and mostly under 10 m/s in velocity. The cusps observed in the GDOP are caused by the evolving relative geometry of the satellites with respect to the payload antenna, causing gradual degradation of observability in the range direction. As the relative geometry evolves, the progressive alignment of the tracked satellites leads to a near-degeneracy of the observability matrix, whereas their subsequent separation restores observability. This phenomenon produces transients lasting up to a few minutes and is seen more commonly and dramatically at high altitudes as the satellite geometry tends to be more clustered.

By contrast, in another time window for the same operation spanning March 3, 2025, 11:22–11:30 UTC (shown in black), PVT solutions are stable during a nearly constant-GDOP timespan, with relatively lower steady-state PVT errors on the order of 0.1–1 km in position and 1–1000 m/s in velocity. The range error continues to dominate the overall solution error, as in OP1_0.

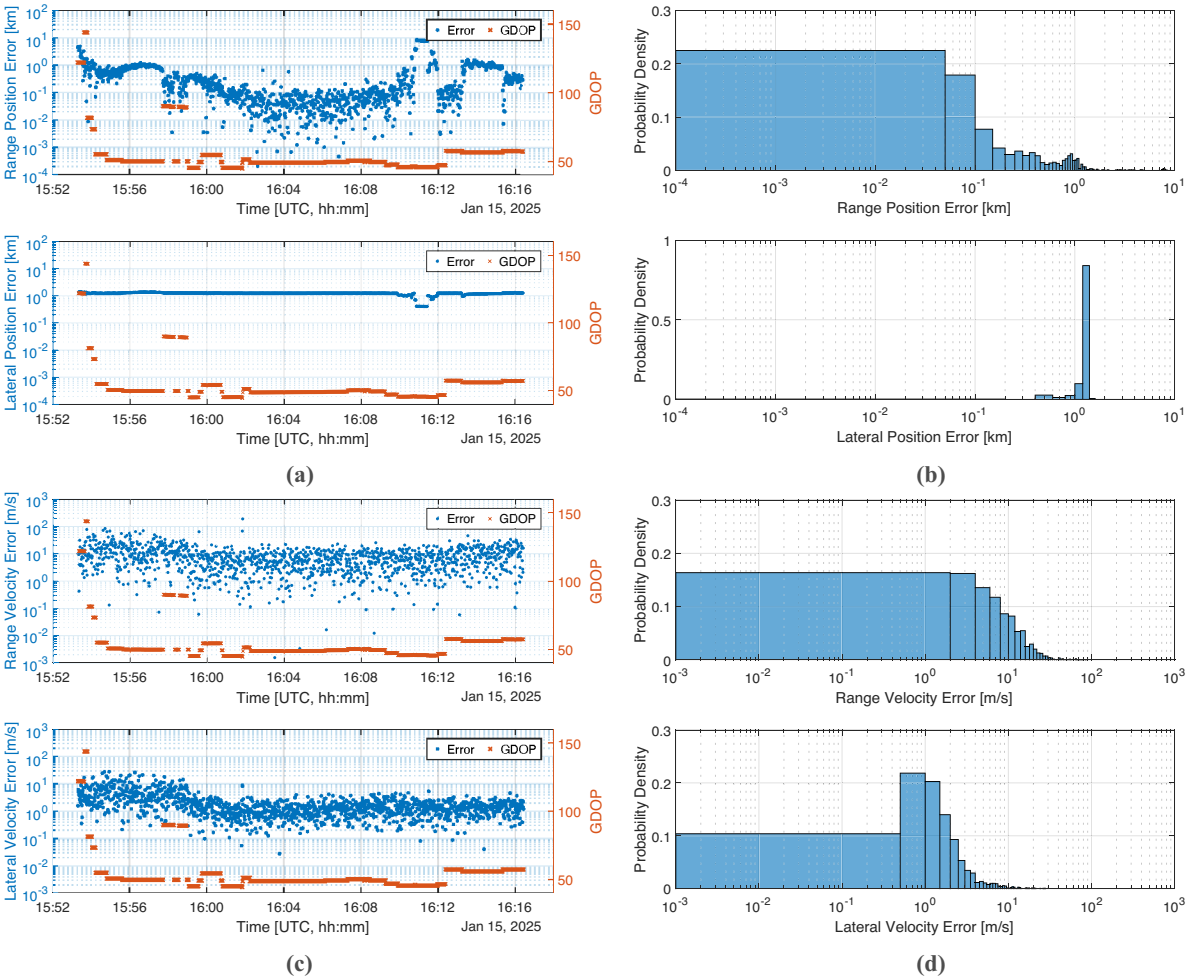

FIGURE 25 OP1_0 (15.03 RE) onboard PVT range and RSS lateral state error from the Firefly definitive trajectory and GDOP value. (a) Range and lateral position error time series, (b) Range and lateral position error probability density, (c) Range and lateral velocity error time series, (d) Range and lateral velocity error probability density.

In general, these results show the feasibility of calculating GNSS least-squares navigation solutions even from the lunar surface, but reveal the inherent limitations to accuracy caused by the geometry of the solution at such a distance. Use for operational navigation should instead focus on sequential navigation solutions, e.g., calculated via a Kalman filter architecture. Furthermore, for high-precision navigation, a user must break the high degree of correlation between the range and clock error. As discussed by Winternitz et al. (2019), this can be done by either using a high-stability clock or including independent measurements that improve the observability of the range component.

5.5 | Characterization of In-Phase/Quadrature Signal Batches

The unique LuGRE IQS data sets, collected on the Moon in both the L1/E1 and L5/E5a bands, provide an unprecedented record of the raw GNSS signal as received in the lunar environment, enabling high-fidelity post-processing for signal characterization, performance verification, environmental assessment,

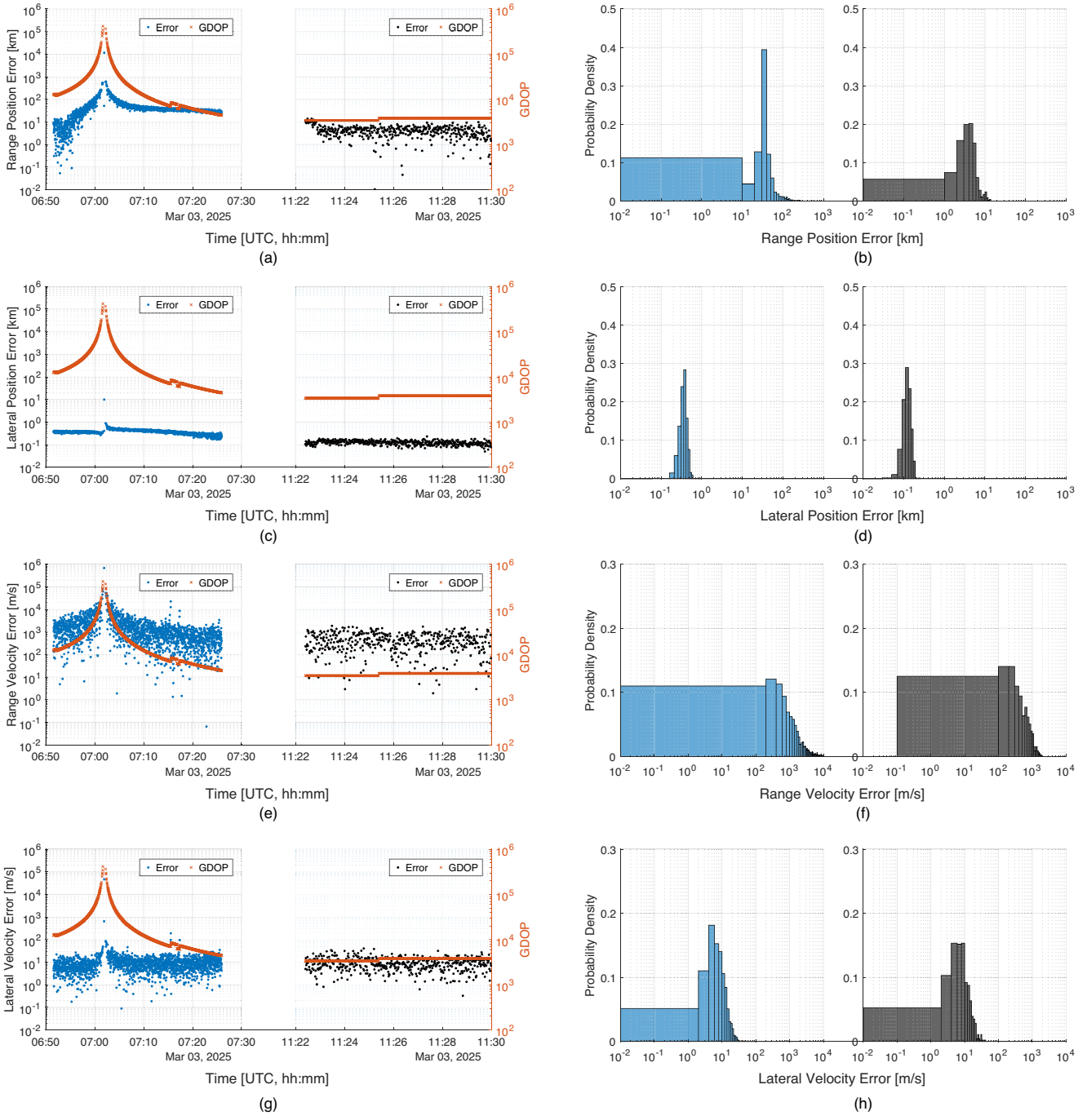

FIGURE 26 OP38_0 (lunar surface) PVT range and RSS lateral state error and GDOP within two different GDOP environments. (a) Range position error time series, (b) Range position error probability density, (c) Lateral position error time series, (d) Lateral position error probability density, (e) Range velocity error time series, (f) Range velocity error probability density, (g) Lateral velocity error time series, (h) Lateral velocity error probability density.
The first window (blue) spans a dynamically changing GDOP environment on the lunar surface, and the second window (black) spans a stable GDOP environment; note the different time scales for each case, which correspond to the duration of each PVT period.

and testing of advanced acquisition and tracking algorithms. Despite their short duration owing to limited data volume and downlink capacity, these batches allow for a spectral analysis of GNSS signals received throughout mission operations.

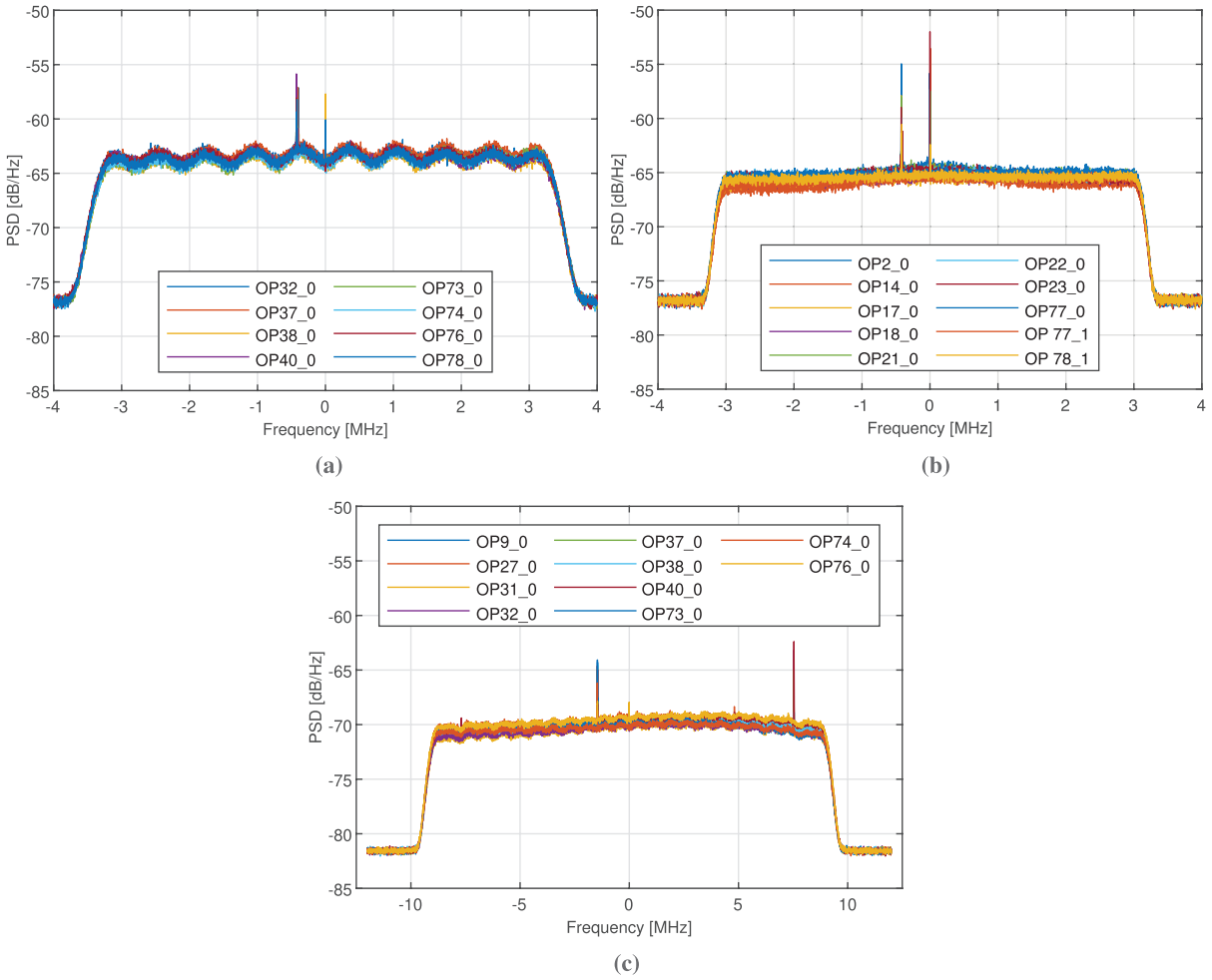

FIGURE 27 Aggregated PSD plots for L1/E1 and L5/E5a IQS batches captured with different payload configurations. (a) L1/E1 signal at 8 Msps and 4 bits; filter A, (b) L1/E1 signal at 8 Msps and 4 bits; filter B, (c) L5/E5a signal at 24 Msps and 4 bits.

To provide an overview of the LuGRE IQS data sets, Figure 27 shows the estimated power spectral density (PSD) under different payload configurations. The PSD is estimated using Welch's method, aggregated by operations using similar SC configurations. The estimation used a 4096-point fast Fourier transform, a rectangular window, and an overlap of 128 samples between successive windows. Because of the low power of GNSS signals, their cumulative spectral density is barely distinguishable and decreases with altitude. The differences in the in-band density levels observed among the PSDs are primarily due to the automatic gain control, which maintains an approximately constant signal power at the input of the analog-to-digital converter.

Depending on the specific settings for the SC mode, different front-end filters resulted in different spectral behavior of the collected samples. In general, one filter (filter A) was used for dual-frequency SCs and for the OP78_0 single-frequency capture. Most single-frequency captures used filter B. As shown in Figure 27(a), captures performed with filter A exhibit pronounced ripples in frequency response induced by the anti-aliasing filter used prior to sample decimation. In fact, all rippling L1/E1 data sets were obtained by decimating 24-Msps SCs by a factor of three, in order to reduce storage requirements and downlink data volume. In contrast, filter B shows a comparatively flat and more uniform response, as these

TABLE 6
Comparison of Estimated C/N_0 and Doppler Shifts for GPS Signals Observed in OP2_0 Pre- and Post-Filtering

Signal, PRN	Est. C/N_0 [dB-Hz]			Doppler shift [kHz]			C/N_0 increase due to filtering (dB)
	IQS	ACQ	Filtered IQS	IQS	ACQ	Filtered IQS	
GPS L1 C/A, 18	39.21	40.81	39.30	−10.800	−12.448	−10.800	0.09
GPS L1 C/A, 24	37.03	40.63	37.19	−3.100	−4.748	−3.100	0.16

data sets were natively recorded at 8 Msps with no further decimation and no anti-aliasing filtering.

Figure 27 also reveals the presence of spurious signal power near the central frequency of each band, likely caused by EMI. Therefore, to assess the integrity of the received files as well as the potential impact on available GNSS signals due to EMI, post-processing of the received batches was performed. As an example, signal acquisition was performed in post-procesing using IQSs of GPS L1 for PRN 18 and PRN 24 during OP2_0, with 5 non-coherent sums, 8 ms of coherent integration time, a Doppler search space of ±20 kHz, and a Doppler step of 50 Hz. The acquisition was considered to be effective when comparison of the estimated C/N_0 and Doppler shift with values obtained through the onboard acquisition (ACQ) performed by the receiver in the subsequent RTP operation showed similar results. As shown in Table 6, the resulting values are considered reasonably close for the target PRNs, excluding the possibility of false acquisition.

Two cascading notch filters were then applied in post-processing to filter out the EMI components; a comparison between pre-filter and post-filter signal strength is shown in the "Filtered IQS" column of Table 6. The resulting C/N_0 increase of 0.09 dB and 0.16 dB without an impact on Doppler shift suggests a negligible impact of EMI during mission operations. Similar preliminary integrity checks were performed throughout the mission for different PRNs and constellations, with no significant issues reported. A deeper analysis is left for future work.

6 | DISCUSSION

The results obtained by LuGRE described in the previous sections demonstrate the successful acquisition and tracking of GNSS signals at the Moon and the formulation of instantaneous PVT solutions, even in the presence of a C/N_0 discrepancy on the order of −7 to −12 dB. Selected specific findings and observations are summarized in the following discussion.

6.1 | Signals

- As predicted by many prior studies and now demonstrated by LuGRE, open signals from GPS and Galileo in the L1 and L5 bands can be readily received, acquired, and tracked at lunar distance and on the Moon's surface when in view of the Earth. This includes a robust quantity of main-lobe signals as well as a substantial quantity of side-lobe signals, which LuGRE was able to acquire only at their peaks, given the C/N_0 discrepancy observed in-flight. Side-lobe signals are especially important for (a) increasing the overall measurement

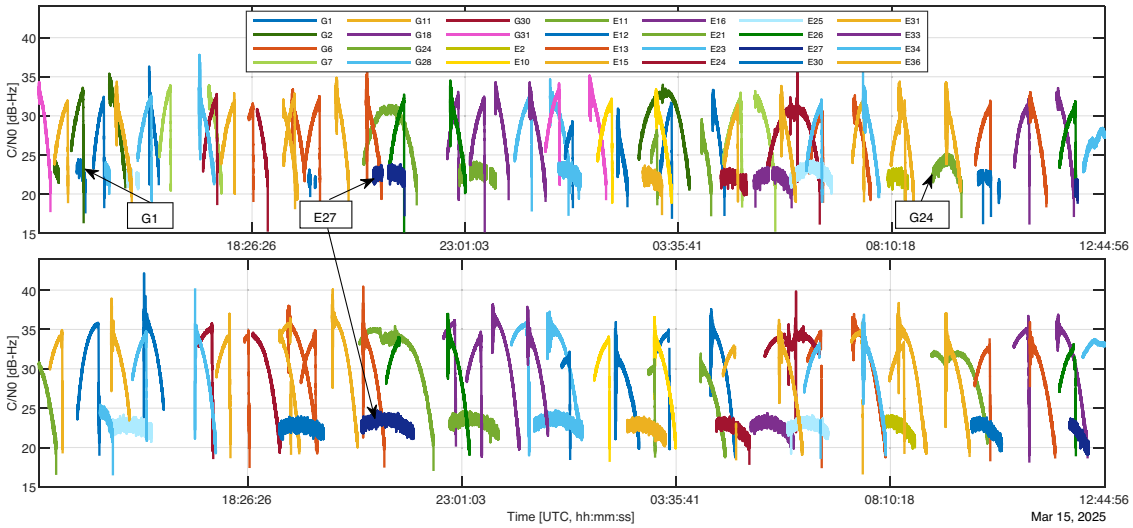

FIGURE 28 Examples of side-lobe signals tracked from the lunar surface during OP74_0 (61.90 RE)
GPS L1 C/A and Galileo E1C are shown on the top; GPS L5Q and Galileo E5a-Q are shown on the bottom.

quantity for navigation and (b) improving measurement continuity through gaps in main-lobe signals.

- The overall availability discussed in Section 5.3 benefits from signals originating from the side-lobes of the GNSS transmit antennas during both transit and surface operations. Figure 28 provides a representative example from surface operations during OP74_0 (61.90-RE altitude and above), during which several side-lobe signals were tracked for both systems and both frequencies. As noted in the figure, side-lobe signals were directly acquired and tracked from GPS PRN 1 (G1) and PRN 24 (G24) on L1 C/A and were tracked from Galileo PRN 27 (E27) on both E1C and E5a-Q. GPS L5 side-lobe signals were tracked at lower altitudes. These observations confirm that side-lobe signals can be effectively acquired and tracked at the lunar surface, improving overall availability.
- The signals that were acquired and tracked are of high quality, with code and phase measurement standard deviations consistent with that of measurements from Earth-vicinity receivers. In particular, the L5 and E5a signals show improved measurement quality over their L1 C/A and E1 OS counterparts. These results are true regardless of altitude or location, whether in transit or on the Moon's surface.
- In general, the L5/E5a band offers substantial benefits in the lunar environment compared with the corresponding L1/E1 band. Improved C/N_0 and a broader main-lobe lead to increased visibility and acquisition opportunities, as demonstrated in Figure 29 for GPS PRN 6 and Galileo PRN 34 for OP17_0. Improved quality leads to a higher likelihood of successful acquisition, stable tracking, and positive contribution to the navigation solution.
- As highlighted by Delépaut et al. (2020), the specific geometry of each constellation affects its visibility from the Moon. LuGRE provided experimental evidence of this phenomenon. For Galileo, which features three highly inclined orbit planes, LuGRE observed a long-term trend in visibility as each plane aligned with the Moon line of sight; Figure 30 shows the Galileo tracked

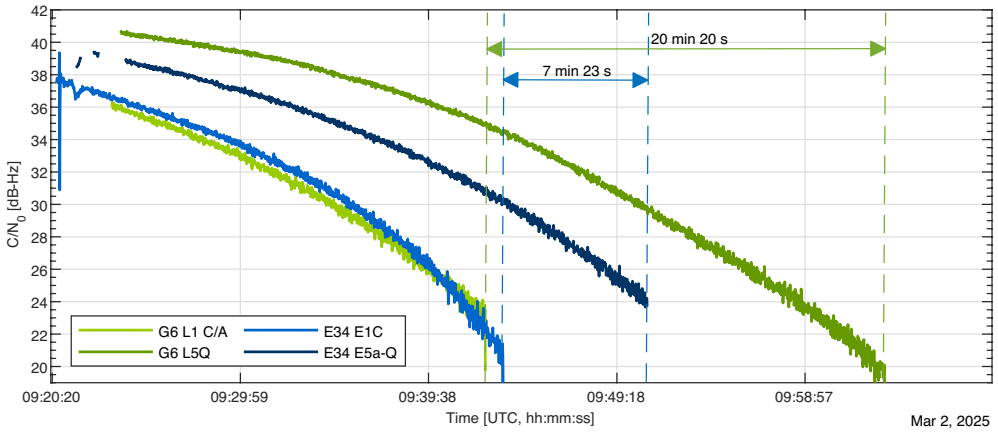

FIGURE 29 L1/E1 and L5/E5a C/N_0 tracking arcs for GPS PRN6 and Galileo PRN 34, as received during OP17_0

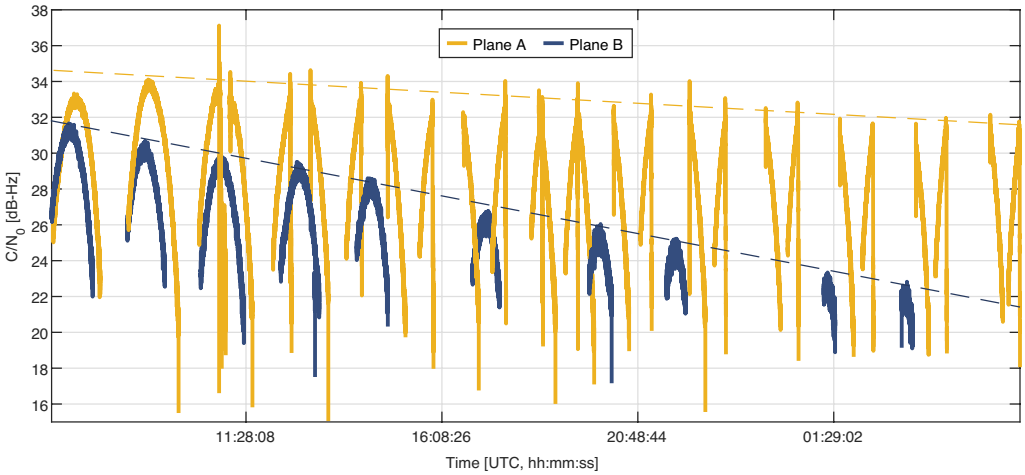

FIGURE 30 Galileo main-lobe signals tracked from the lunar surface during OP38_0 over approximately 24 h
Dashed lines show the linearly interpolated trend of C/N_0 maxima for the different orbital planes (i.e., A and B).

C/N_0 over a nearly 24-h period during OP38_0 on the lunar surface. In this case, main-lobe signals from Galileo PRNs 34, 15, 13, 26, 33, 10, and 36 are all tracked, but at progressively lower signal strength as their common orbit plane aligns with the LuGRE line of sight, eventually falling below the acquisition threshold of the receiver (as affected by the present C/N_0 discrepancy). Other Galileo signals in other orbit planes are not affected. GPS does not show this long-term behavior as markedly, as its satellites are distributed across six orbit planes. This result implies that GNSS signal visibility, especially for Galileo, will show a long-term oscillation, especially if primarily main-lobe signals are used.

- Interactions between GNSS signals and the ionosphere are well known, to the extent that these interactions form the basis for the field of GNSS radio occultation (Angling et al., 2021; Wu et al., 2024). These effects are visible from lunar distances as well and must be considered by lunar GNSS applications. Figure 31 shows an example of degraded C/N_0 measurements as the signals (in this case, from Galileo PRN 36) travel through the ionosphere at a grazing

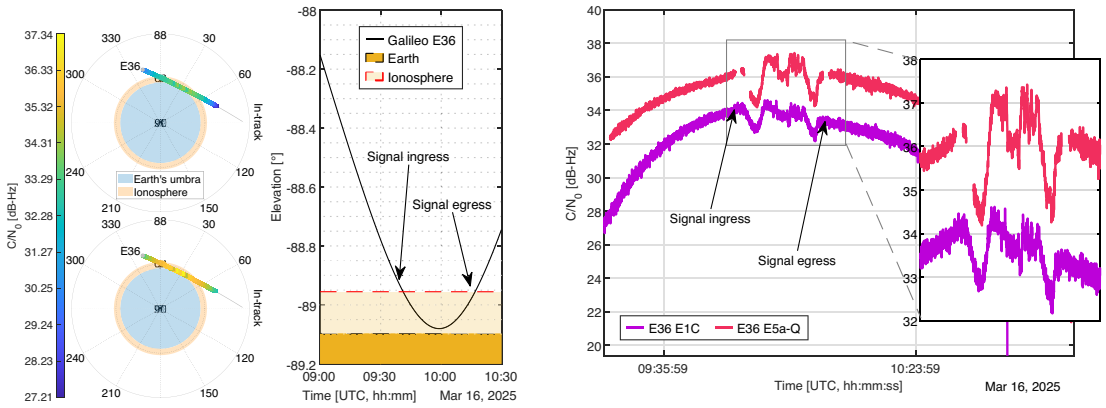

FIGURE 31 Galileo main-lobe signals showing effects on C/N_0 measurements when traversing the Earth ionosphere during OP76_0. (a) E36 E1/E5a space skyplot, (b) E36 elevation, (c) Signature of ionospheric occultation on E36 E1/E5 pilot signals.

altitude as low as 50 km above the Earth's surface. The observed C/N_0 shows a distinct signature, marked by pronounced fluctuations immediately after signal ingress and just before signal egress. Although this pattern remains recognizable in other operational contexts, it is most often interrupted by Earth occultation. An example of such a discontinuity is shown for Galileo PRN 34 (E34 E1 and E5a) in Figure 29, where both E1 and E5a signals were first tracked only after signal egress.

6.2 | Payload Design

- In general, multi-constellation and multi-frequency capabilities greatly enhance performance in this environment, primarily by increasing signal availability and measurement quantity. Increasing the capability of lunar receivers to support additional GNSS constellations and signals can be shown by analysis to be beneficial, and LuGRE demonstrates this benefit in practice. For example, during a 24-h period on the lunar surface (OP38_0), multi-fold (2+) signal availability increased from 25% for a dual-frequency GPS-only scenario to nearly 70% with both GPS and Galileo included (see Figures 22–24). Similarly, Table 5 shows gains in 4+ signal availability with the inclusion of L5/E5a in addition to L1/E1.
- In any weak-signal environment, especially at lunar distances, the C/N_0 margin is low, and signal visibility and thus navigation availability are greatly impacted by marginal link budget effects. The large C/N_0 discrepancy observed by LuGRE is under investigation, but highlights the need for a robust link budget margin, careful calibration of the payload link budget before flight, and root cause analysis for any observed discrepancies.
- Because of the inherent benefits of the L5/E5a signals, receivers can benefit by acquiring these signals directly, rather than using L1/E1 as an acquisition aid. This approach will improve the ease of acquisition as each PRN comes into view and will improve the overall measurement quantity, as the L5/E5a signal tends to be available above a given receiver C/N_0 threshold longer and earlier than the corresponding L1/E1 signal.

- If demanding navigation performance requirements are levied, a high-stability clock is likely necessary. LuGRE saw successful acquisition and tracking using a commercial-grade VCTCXO, but did not have specific requirements for navigation accuracy. Previous studies point to the need for high-stability clocks for high-precision real-time navigation (Winternitz et al., 2019).
- A robust aiding approach is beneficial in numerous scenarios, including during non-continuous operations, as in the LuGRE transit phase, or during continuous operations in lunar orbit, when occultations may periodically interrupt the line of sight. As described in Section 3.2, LuGRE used aiding of time, its own ephemeris, and GNSS constellation ephemerides and was thus enabled to quickly acquire the signal when started. Accepting some or all of these aiding inputs adds flexibility to the system. At a minimum, accepting an uploaded constellation ephemeris is likely the most important, as the ability to obtain ephemeris demodulated from the signal itself is degraded with a lower C/N_0. In the LuGRE case, lander ephemeris aiding added a high degree of operational complexity, and time aiding imposed additional requirements on the host vehicle that may not be reasonable in other cases.

6.3 | Operations

- Continuous, long-duration operations are an obvious advantage of GNSS navigation, as it allows time for cold-start acquisition; allows for stabilization of payload hardware, especially clock drift; enables long-duration tracking arcs to be maintained for each acquired PRN; and allows for full convergence of a navigation filter. This approach depends on the availability of a GNSS antenna that can be pointed at will and to the necessary accuracy of the user's system.
- If continuous operations cannot be achieved, powering the payload components well in advance of the start of processing is useful, as it allows for warm-up and stabilization of the components, especially the clock. For example, Figure 5 shows the 10- to 15-min clock drift transient observed during the LuGRE receiver power-on. Situations requiring rapid navigation convergence may especially benefit from this practice.

6.4 | Navigation

- Use of a navigation filter is critical for robust navigation in the lunar environment, considering the relative sparsity of instantaneous PVT solutions and the poor geometry associated with lunar-distance signal reception. Such a filter should implement best practices, including the option to exclude measurements from signals for which the height of the ray path (or grazing altitude) is below a threshold and to automatically edit measurements for outliers and visibility constraints (Carpenter & D'Souza, 2025).
- Utilizing current Earth orientation parameter data is critical for high-accuracy navigation at lunar distances, as errors can increase to the level of hundreds of meters in coordinate frame rotations if incorrect or outdated values are used. These values can be provided via telecommand, as was the case for LuGRE, or by supporting broadcast ephemeris messages containing these data, such as the GPS Civil Navigation (CNAV) message on its L5 signal.

7 | CONCLUSIONS

LuGRE successfully demonstrated GNSS signal acquisition, tracking, and navigation at the Moon, having completed its operational mission as part of the Firefly BGM1 from January 15 to March 16, 2025, and having met all top-level scientific requirements. The previous sections described the background, objectives, and requirements of the mission; the technical details of the payload and its ground system; the operational mission experience and collected data; the top-level scientific results; and observations and findings of use for future developers of lunar GNSS receiver systems. These sections represent a first look at the key results of the mission, to be explored further in future work.

LuGRE demonstrated that GNSS signals from the GPS and Galileo can be acquired and tracked in cislunar space, in lunar orbit, and on the Moon's surface and demonstrated real-time navigation using those signals via instantaneous least-squares point solutions. Further, the LuGRE results show that those signals are of sufficient power and quality to support future operational use for cislunar navigation, given capable receiver equipment. The LuGRE team hopes that this demonstration and the public data set provided build confidence in GNSS as a lunar PNT capability and accelerate its use for future lunar applications.

8 | PUBLIC DATA SET

The public LuGRE mission data set is available at https://doi.org/10.5281/zenodo.16411686. This data set consists of releasable documentation, ancillary data, and payload telemetry, with the latter provided in raw form and packaged in standard formats to promote rapid utilization (Parker et al., 2025). The data consist, at a minimum, of the products described in Table 7.

To support the use of LuGRE data by the scientific community, an open-source analysis tool has been developed (Minetto et al., 2025) and made publicly available at https://github.com/NavsasPolito/LuNART.

TABLE 7
LuGRE Minimum Public Data Products

ID	Level[a]	Description	Coverage
TLM_ACQ	L0	Receiver ACQ (acquisition) message, in raw binary and text forms	All RTP operations, 1-Hz rate
TLM_RAW	L0	Receiver RAW (measurements) message, in raw binary and text forms	All RTP operations, 1-Hz rate
TLM_NAV	L0	Receiver NAV (least-squares PVT solutions) message, in raw binary and text forms	All RTP operations, 1-Hz rate
IQS_L1	L0	I/Q SC binary data, L1 and E1 bands	All SC operations (variable parameters)
IQS_L5	L0	I/Q SC binary data, L5 and E5a bands	All SC operations (variable parameters)
OPTABLE	Ancillary	Detailed operations table	Full mission
ICD	Ancillary	Binary data format interface control document	N/A

[a] Product levels are aligned with definitions in the NASA Science Mission Directorate (2022), Appendix E.

ACKNOWLEDGMENTS

The LuGRE team would like to extend heartfelt thanks to the following individuals whose contributions truly made this mission possible. The team also wishes to thank the Firefly team, our interfaces in the NASA Commercial Lunar Payload Services, and all of the colleagues and external advisors who helped along the way.

NASA

Benjamin Anderson
Bill Bamford
Frank Bauer
Cory Heiges
Kendall Mauldin
John McCloskey
Stephen McKim
James J. Miller
Siddartha Sanathanamurthy
Lisa Valencia

ASI

Luigi Ansalone
Giuseppe D'Amore
Tommaso Pino
Danilo Vicari
Gabriele Impresario
Francesca Paccagnini
Eliane Sangermani

Qascom

Simone Tedesco
Salvatore Guzzi
Giovanni Campagnolo
Matteo Pulliero
Mattia Ghedin
Davide Martini
Nicola Montini
Federica Rozzi
Luca Canzian
Alessandro Pozzobon
Oscar Pozzobon

Politecnico di Torino

Francesco Fiorina
Luca Morichi
Lorenzo Sciacca

REFERENCES

Angling, M. J., Nogués-Correig, O., Nguyen, V., Vetra-Carvalho, S., Bocquet, F.-X., Nordstrom, K., Melville, S. E., Savastano, G., Mohanty, S., & Masters, D. (2021). Sensing the ionosphere with the Spire radio occultation constellation. *Journal of Space Weather and Space Climate*, *11*, 56. https://doi.org/10.1051/swsc/2021040

Anthony, T. (2022a, August). *NAVSTAR GPS space segment / navigation user segment interfaces (IS-GPS-200)*. https://www.navcen.uscg.gov/sites/default/files/pdf/gps/IS-GPS-200N.pdf

Anthony, T. (2022b, August). *NAVSTAR GPS space segment / user segment L5 interfaces (IS-GPS-705)*. https://www.navcen.uscg.gov/sites/default/files/pdf/gps/IS-GPS-705J.pdf

Ashman, B., Bauer, F. H., Parker, J., & Donaldson, J. (2018). GPS operations in high earth orbit: Recent experiences and future opportunities. In *2018 SpaceOps Conference*. https://doi.org/10.2514/6.2018-2568

Ashman, B., Schlenker, L., Parker, J. J., Bauer, F., Winternitz, L., Long, A., Craft, K., & Hassouneh, M. (2021). Applications and benefits of GNSS for lunar exploration. In *2021 SpaceOps Conference*. https://ntrs.nasa.gov/citations/20210014049

Ashman, B. W., Winternitz, L. B., Stacey, N. I., Long, A. C., Schmidt, M. C., Ryden, G. A., Liounis, A. J., Price, S. R., Bamford, W. A., Hur-Diaz, S. H., Hassouneh, M. A., & Greenlee, L. A. (2024, September). Autonomous navigation of a lunar relay using GNSS and other measurements. In *Proceedings of the 37th International Technical Meeting of the Satellite Division of the Institute of Navigation (ION GNSS+ 2024)*, 3156–3173. https://doi.org/10.33012/2024.19673

Balbach, O., Eissfeller, B., Hein, G., Enderle, W., Schmidhuber, M., & Lemke, N. (1998). Tracking GPS above GPS satellite altitude: First results of the GPS experiment on the HEO mission Equator-S. In *IEEE 1998 Position Location and Navigation Symposium (Cat. No.98CH36153)*, 243–249. https://doi.org/10.1109/PLANS.1998.670065

Bauer, F., Moreau, M., Dahle-Melsaether, M., Petrofski, W., Stanton, B., Thomason, S., Harris, G. A., Sena, R., & Temple, L. P. I. (2006, September). The GPS space service volume. In *Proceedings of the 19th International Technical Meeting of the Satellite Division of the Institute of Navigation (ION GNSS 2006)*, 2503–2514. https://www.ion.org/publications/abstract.cfm?articleID=6861

Betz, J. W. (2015). *Engineering satellite-based navigation and timing: Global navigation satellite systems, signals, and receivers*. Wiley-IEEE Press. https://doi.org/10.1002/9781119141167

Betz, J. W., & Kolodziejski, K. R. (2000). Extended theory of early-late code tracking for a bandlimited GPS receiver. *Navigation*, *47*(3), 211–226. https://doi.org/10.1002/j.2161-4296.2000.tb00215.x

Carpenter, J. R., & D'Souza, C. N. (2025, March). *Navigation filter best practices* (Technical Publication). National Aeronautics and Space Administration. https://ntrs.nasa.gov/citations/20250002787

Croissant, K., Jenkins, G., McKnight, R., Peters, B. C., Ugazio, S., & van Graas, F. (2021, January). Bobcat-1, the Ohio University CubeSat: Preliminary data analysis. In *Proceedings of the 2021 International Technical Meeting of the Institute of Navigation*, 625–636. https://doi.org/10.33012/2021.17854

CYGNSS. (2024). *CYGNSS level 1 science data record version 3.2*. Retrieved September 2, 2025, from https://doi.org/10.5067/CYGNS-L1X32

Das, P., Ortega, L., Vilà-Valls, J., Vincent, F., Chaumette, E., & Davain, L. (2020). Performance limits of GNSS code-based precise positioning: GPS, Galileo & meta-signals. *Sensors*, *20*(8), 2196. https://doi.org/10.3390/s20082196

Delépaut, A., Giordano, P., Ventura-Traveset, J., Blonski, D., Schönfeldt, M., Schoonejans, P., Aziz, S., & Walker, R. (2020). Use of GNSS for lunar missions and plans for lunar in-orbit development [Scientific and fundamental aspects of GNSS - Part 1]. *Advances in Space Research*, *66*(12), 2739–2756. https://doi.org/10.1016/j.asr.2020.05.018

European Union. (2023, November). *European GNSS (Galileo) open service, signal-in-space interface control document (OS SIS ICD V2.1)*. https://www.gsc-europa.eu/sites/default/files/sites/all/files/Galileo_OS_SIS_ICD_v2.0.pdf

Fantinato, S., Miotti, E., Bernardi, F., Guzzi, S., Tedesco, S., Campagnolo, G., Pozzobon, O., Facchinetti, C., Musumeci, M., Parker, J. J. K., Konitzer, L., Dovis, F., & Minetto, A. (2025, September). Moon GNSS positioning. *Presented at the 38th International Technical Meeting of the Satellite Division of the Institute of Navigation (ION GNSS+)*. https://www.ion.org/gnss/abstracts.cfm?paperID=16128

Fantinato, S., Miotti, E., Boschiero, M., Bartolucci, M., Bergamin, M., Marcantonio, D., Pulliero, M., Rozzi, F., & Pozzobon, O. (2022, September). Development challenges of a GNSS SDR receiver for moon landing. In *Proceedings of the 35th International Technical Meeting of the Satellite Division of the Institute of Navigation (ION GNSS+ 2022)*, 602–627. https://doi.org/10.33012/2022.18369

Fiorina, F., Vouch, O., Nardin, A., Dovis, F., Facchinetti, C., & Musmeci, M. (2025, April 28–May 01). A sequence matching approach for GNSS-based orbit determination using dynamic time warping. In *Proceedings of the 2025 IEEE/ION Position, Location and Navigation Symposium (PLANS)*, Utah, 1055–1065. https://doi.org/10.1109/PLANS61210.2025.11028519

Giordano, P., Malman, F., Swinden, R., Zoccarato, P., & Ventura-Traveset, J. (2022, January). The lunar pathfinder PNT experiment and moonlight navigation service: The future of lunar position, navigation and timing. In *Proceedings of the 2022 International Technical Meeting of the Institute of Navigation*, 632–642. https://doi.org/10.33012/2022.18225

Guzzi, S., Longo, R., Bernardi, F., Fantinato, S., Pozzobon, O., Miller, J. J., Valencia, L., De Leon, P., Facchinetti, C., & Musmeci, M. (2025, September). GARSPACE GNSS receiver experimentation results during SL-15 sounding rocket launch. In *Proceedings of the 38th International Technical Meeting of the Satellite Division of the Institute of Navigation (ION GNSS+ 2025)*. https://doi.org/10.33012/2025.20421

Hassouneh, M. A., Midkiff, D., Winternitz, L. M., Price, S. R., Thomas, L., Hatke, D., Lee, T., Bamford, W., & Mitchell, J. W. (2023, September). NavCube3-mini lunar GNSS receiver. In *Proceedings of the 36th International Technical Meeting of the Satellite Division of the Institute of Navigation (ION GNSS+ 2023)*, 3540–3548. https://doi.org/10.33012/2023.19343

International Space Exploration Coordination Group (ISECG). (2024, August). *International space exploration coordination group global exploration roadmap*. https://www.globalspaceexploration.org/wp-content/isecg/GER2024.pdf

Israel, D. J., Mauldin, K. D., Roberts, C. J., Mitchell, J. W., Pulkkinen, A. A., Cooper, L. V. D., Johnson, M. A., Christe, S. D., & Gramling, C. J. (2020, March). LunaNet: A flexible and extensible lunar exploration communications and navigation infrastructure. In *2020 IEEE Aerospace Conference*, 1–14. https://doi.org/10.1109/AERO47225.2020.9172509

Jiang, Y. (2025, February). Conception of lunar PNT. In *Joint ICG-IOAG Multilateral Cislunar PNT Workshop*. https://ioag.org/Cislunar%20PNT%20Workshop/1b.%20Overview%20of%20Lunar%20PNT%20Frameworks%20%26%20Systems%20(Part%20II)/02%20Conception%20of%20Lunar%20PNT.pdf

Joo, J. M. (2025, February). Korean cislunar PNT. In *Joint ICG-IOAG Multilateral Cislunar PNT Workshop*. https://ioag.org/Cislunar%20PNT%20Workshop/1b.%20Overview%20of%20Lunar%20PNT%20Frameworks%20%26%20Systems%20(Part%20II)/04%20250211_Cislunar%20Workshop_Korean%20Cislunar%20PNT_jmjoo.pdf

Kaplan, E. D., & Hegarty, C. (2017). *Understanding GPS/GNSS: Principles and applications*. Artech House.

Konitzer, L., Esantsi, N., & Parker, J. (2022, August). Navigation performance analysis and trades for the lunar GNSS receiver experiment (LuGRE). In *2022 AAS/AIAA Astrodynamics Specialist Conference*, (AAS 22-642). https://ntrs.nasa.gov/citations/20220010106

Konitzer, L., Parker, J. J. K., Ashman, B., Esantsi, N., Facchinetti, C., Dovis, F., Minetto, A., Nardin, A., Bauer, F., Ansalone, L., & Impresario, G. (2024, September). Science objectives and investigations for the lunar GNSS receiver experiment (LuGRE). In *Proceedings of the 37th International Technical Meeting of the Satellite Division of the Institute of Navigation (ION GNSS+ 2024)*, 1061–1081. https://doi.org/10.33012/2024.19711

Long, A. C., & Stacey, N. (2025). *Goddard Enhanced Onboard Navigation System (GEONS) 3.1 Mathematical Specifications*. NASA Goddard Space Flight Center Technical Report, NASA/TP-20250006484.

Medina, D., Ortega, L., Vilà-Valls, J., Closas, P., Vincent, F., & Chaumette, E. (2020). Compact CRB for delay, Doppler, and phase estimation – application to GNSS SPP and RTK performance characterisation. *IET Radar, Sonar & Navigation*, *14*(10), 1537–1549. https://doi.org/10.1049/iet-rsn.2020.0168

Menzione, F., Sgammini, M., & Paonni, M. (2024). *Reconstruction of Galileo Constellation Antenna Pattern for space service volume applications* (KJ-NA-31-812-EN-N). Publications Office of the European Union. https://doi.org/10.2760/765842

Minetto, A., Zocca, S., Vouch, O., Nardin, A., Dovis, F., Musmeci, M., & Facchinetti, C. (2025, September). LuNART-q: The LuGRE quick navigation analysis and reporting tool. In *Proceedings of the 38th International Technical Meeting of the Satellite Division of the Institute of Navigation (ION GNSS+ 2025)*, 1377–1390. https://doi.org/10.33012/2025.20440

Nardin, A., Minetto, A., Guzzi, S., Dovis, F., Konitzer, L., & Parker, J. (2023, September). Snapshot tracking of GNSS signals in space: A case study at lunar distances. In *Proceedings of the 36th International Technical Meeting of the Satellite Division of the Institute of Navigation (ION GNSS+ 2023)*, 3267–3281. https://doi.org/10.33012/2023.19174

Nardin, A., Minetto, A., Vouch, O., Mariani, M., & Dovis, F. (2022, September). Snapshot acquisition of GNSS signals in space: A case study at lunar distances. In *Proceedings of the 35th International Technical Meeting of the Satellite Division of the Institute of Navigation (ION GNSS+ 2022)*, 3603–3617. https://doi.org/10.33012/2022.18477

NASA Science Mission Directorate. (2022, September 26). *Scientific information policy for the science mission directorate SMD policy document SPD-41a* (Policy Document No. SPD-41a). NASA Science Mission Directorate. https://science.nasa.gov/wp-content/uploads/2023/08/smd-information-policy-spd-41a.pdf

U.S. Coast Guard Navigation Center (NAVCEN). (2025). *GPS technical reports*. U.S. Department of Homeland Security. https://www.navcen.uscg.gov/gps-technical-references

Parker, J. J. K., Dovis, F., Anderson, B., Ansalone, L., Ashman, B., Bauer, F. H., D'Amore, G., Facchinetti, C., Fantinato, S., Impresario, G., McKim, S. A., Miotti, E., Miller, J. J., Musmeci, M., Pozzobon, O., Schlenker, L., Tuozzi, A., & Valencia, L. (2022, January). The lunar GNSS receiver experiment (LuGRE). In *Proceedings of the 2022 International Technical Meeting of the Institute of Navigation*, 420–437. https://doi.org/10.33012/2022.18199

Parker, J. J. K., Dovis, F., Pozzobon, O., Facchinetti, C., Anderson, B., Ansalone, L., Ashman, B., Bauer, F. H., Bernardi, F., Boschiero, M., Campagnolo, G., D'Amore, G., Fantinato, S., Fiorina, F., Ghedin, M., Guzzi, S., Heighes, C., Impresario, G., Konitzer, L., . . . Zocca, S. (2025, October). *Lunar GNSS receiver experiment (LuGRE) mission data* (Version v1). National Aeronautics and Space Administration, Agenzia Spaziale Italiana. https://doi.org/10.5281/zenodo.16411687

Powell, T. D., Martzen, P. D., Sedlacek, S. B., Chao, C.-C., Silva, R., Brown, A., & Belle, G. (1999, January). GPS signals in a geosynchronous transfer orbit: "Falcon Gold" data processing. In *Proceedings of the 1999 National Technical Meeting of the Institute of Navigation*, 575–585. https://www.ion.org/publications/abstract.cfm?articleID=709

Pulliero, M., Cittadin, G., Boschiero, M., Ghedin, M., Marcantonio, D., Fantinato, S., Miotti, E., & Pozzobon, O. (2023, September). The space qualification process of the LuGRE GNSS payload. In *2023 IEEE International Conference on Wireless for Space and Extreme Environments (WiSEE)*, 7–12. https://doi.org/10.1109/WiSEE58383.2023.10289430

Ribot, M. A., Botteron, C., & Farine, P.-A. (2016). Derivation of the Cramér-Rao bound in the GNSS-reflectometry context for static, ground-based receivers in scenarios with coherent reflection. *Sensors*, *16*(12), 2063. https://doi.org/10.3390/s16122063

Sciacca, L., Minetto, A., Nardin, A., Tedesco, S., Boschiero, M., Fantinato, S., Canzian, L., & Dovis, F. (2025, April 28–May 01). Acquiring GNSS signals in cislunar space: A hardware-in-the-loop investigation for LuGRE mission data. In *2025 IEEE/ION Position, Location and Navigation Symposium (PLANS)*, 1036–1045. https://doi.org/10.1109/PLANS61210.2025.11028293

Shukla, A. K. (2025, February). Pseudolite system for lunar PNT. In *Joint ICG-IOAG Multilateral Cislunar PNT Workshop*. https://ioag.org/Cislunar%20PNT%20Workshop/1b.%20Overview%20of%20Lunar%20PNT%20Frameworks%20%26%20Systems%20(Part%20II)/03%20Pseudolite%20System%20for%20Lunar%20PNT_Cislunar_Workshop_11_Feb2025_Ashish_ISRO_FINAL.pdf

Steigenberger, P., Thoelert, S., Dach, R., & Montenbruck, O. (2024). Validation of GPS III transmit antenna calibrations. *Advances in Space Research*, *73*(5), 2488–2498. https://doi.org/10.1016/j.asr.2023.11.048

Steigenberger, P., Thoelert, S., & Montenbruck, O. (2018). GNSS satellite transmit power and its impact on orbit determination. *Journal of Geodesy*, *92*(6), 609–624. https://doi.org/10.1007/s00190-017-1082-2

Tedesco, S., Bernardi, F., Guzzi, S., Boschiero, M., Pulliero, M., Marcantonio, D., Ghedin, M., Miotti, E., Fantinato, S., Pozzobon, O., Facchinetti, C., Musmeci, M., D'Amore, G., Varacalli, G., Minetto, A., Dovis, F., Parker, J. J. K., McKim, S. A., Konitzer, L., . . . Bauer, F. (2023, September). Deep space GNSS in moon transfer orbit: The LuGRE receiver. In *2023 IEEE International Conference on Wireless for Space and Extreme Environments (WiSEE)*, 1–6. https://doi.org/10.1109/WiSEE58383.2023.10289183

United Nations Office for Outer Space Affairs. (2021, September). *The interoperable global navigation satellite systems space service volume* (2nd ed.) (ST/SPACE/75/REV.1). https://docs.un.org/en/st/SPACE/75/REV.1

Vouch, O., Morichi, L., Zocca, S., Minetto, A., & Dovis, F. (2025, April 28–May 01). GNSS precise point positioning in cislunar space: A study on regularized least squares and availability. In *2025 IEEE/ION Position, Location and Navigation Symposium (PLANS)*, 1014–1025. https://doi.org/10.1109/PLANS61210.2025.11028416

Vouch, O., Nardin, A., Minetto, A., Zocca, S., Dovis, F., Konitzer, L., J.K. Parker, J., Bernardi, F., Tedesco, S., & Fantinato, S. (2024, September). Advancing autonomous navigation: Near-Moon GNSS-based orbit determination. In *Proceedings of the 37th International Technical Meeting of the Satellite Division of the Institute of Navigation (ION GNSS+ 2024)*, 3277–3291. https://doi.org/10.33012/2024.19814

Vouch, O., Nardin, A., Minetto, A., Zocca, S., Valvano, M., & Dovis, F. (2024). Aided Kalman filter models for GNSS-based space navigation. *IEEE Journal of Radio Frequency Identification*, *8*, 535–546. https://doi.org/10.1109/JRFID.2024.3403914

Wang, T., Ruf, C. S., Block, B., McKague, D. S., & Gleason, S. (2019). Design and performance of a GPS constellation power monitor system for improved CYGNSS L1B calibration. *IEEE Journal of Selected Topics in Applied Earth Observations and Remote Sensing*, *12*(1), 26–36. https://doi.org/10.1109/JSTARS.2018.2867773

Winternitz, L., Bamford, W., Long, A., & Hassouneh, M. (2019, February). GPS based autonomous navigation study for the Lunar Gateway. In *Proceedings of the Annual American Astronautical Society (AAS) Guidance, Navigation, and Control Conference*, (AAS 19-096). https://ntrs.nasa.gov/citations/20190002311

Winternitz, L. B., Bamford, W. A., & Price, S. R. (2017, September). New high-altitude GPS navigation results from the Magnetospheric Multiscale Spacecraft and simulations at lunar distances. In *Proceedings of the 30th International Technical Meeting of the Satellite Division of the Institute of Navigation (ION GNSS+ 2017)*, 1114–1126. https://doi.org/10.33012/2017.15367

Won, J.-H., & Pany, T. (2017). Signal processing. In P. J. Teunissen & O. Montenbruck (Eds.), *Springer handbook of global navigation satellite systems* (pp. 401–442). Springer International Publishing. https://doi.org/10.1007/978-3-319-42928-1_14

Wu, M. J., Yue, H. Y., Guo, P., Ma, X., Li, H. G., Dong, J. J., & Zuo, F. F. (2024). The initial assessment of ionospheric radio occultation data of MSS-1 satellite and its applications in scintillation exploration. *Earth and Space Science*, *11*(9). https://doi.org/10.1029/2024EA003695

How to cite this article: Parker, J.J.K., Dovis, F., Konitzer, L., Esantsi, N., Ashman, B., Minetto, A., Nardin, A., Vouch, O., Zocca, S., Bernardi, F., Boschiero, M., Fantinato, S., Miotti, E., Facchinetti, C., Musmeci, M., and Varacalli, G. (2026). GNSS reception at the Moon: First results of the lunar GNSS receiver experiment (LuGRE). *NAVIGATION*, *73*. https://doi.org/10.33012/navi.756

APPENDIX A | OPERATIONS CATALOG

TABLE 8
LuGRE Payload Operations: Summary Catalog

OP ID	Phase	Altitude[a] (RE)	Day of Year (2025)	SC_Start[b]	RTP_Start[c]	RTP_End[c]	Mode	SC Configuration
1_0	Commissioning	15.03	015	N/A	15:29:17	16:16:26	RTP	N/A
2_0	Commissioning	25.25	016	01:31:17	01:36:47	02:23:58	SC-RTP	4 bit, 8 Msps L1/E1, 400 ms
3_0	Transit	40.20	017	N/A	02:24:09	03:21:55	RTP	–
4_1[d]	Transit	49.32	018	09:00:54	N/A	N/A	SC	8 bit, 12 Msps L1/E1, 200 ms 8 bit, 24 Msps L5/E5a, 200 ms
5_0	Transit	51.69	019	04:52:11	04:57:41	05:49:50	SC-RTP	8 bit, 8 Msps L1/E1, 200 ms
9_0	Transit	34.88	025	05:08:24	05:14:06	06:06:01	SC-RTP	4 bit, 24 Msps L5/E5a, 200 ms
12_0	Transit	39.93	030	04:25:09	04:30:39	05:22:47	SC-RTP	4 bit, 4 Msps L1/E1, 800 ms
14_0	Transit	29.91	030	22:40:56	22:46:25	23:38:33	SC-RTP	4 bit, 8 Msps L1/E1, 400 ms
17_0	Transit	44.91	034	09:13:40	09:19:10	10:11:21	SC-RTP	4 bit, 8 Msps L1/E1, 400 ms
18_0	Transit	49.55	036	22:59:10	23:04:39	23:56:49	SC-RTP	4 bit, 8 Msps L1/E1, 600 ms
21_0	Transit	32.63	038	23:29:01	23:34:39	00:26:48^{+1}	SC-RTP	4 bit, 8 Msps L1/E1, 600 ms
22_0	Transit	52.92	043	03:47:55	02:53:12	03:45:35	RTP-SC	4 bit, 8 Msps L1/E1, 400 ms
23_0	Lunar Orbit	61.19	045	04:58:53	04:04:10	04:56:32	RTP-SC	4 bit, 8 Msps L1/E1, 400 ms
27_0	Lunar Orbit	62.18	050	15:22:50	15:28:18	16:20:27	SC-RTP	4 bit, 24 Msps L5/E5a, 200 ms
31_0	Lunar Orbit	60.13	054	03:40:19	N/A	N/A	SC	4 bit, 24 Msps L5/E5a, 200 ms
32_0	Lunar Orbit	58.93	055	12:04:49	N/A	N/A	SC	4 bit, 8 Msps L1/E1, 300 ms 4 bit, 24 Msps L5/E5a, 300 ms
37_0	Lunar Orbit	56.44	058	16:09:37	16:15:46	17:07:14	SC-RTP	4 bit, 8 Msps L1/E1, 300 ms 4 bit, 24 Msps L5/E5a, 300 ms
38_0	Surface	55.85	062	06:13:00	06:19:09	06:10:41^{+1}	SC-RTP	4 bit, 8 Msps L1/E1, 300 ms 4 bit 24 Msps L5/E5a, 300 ms
40_0	Surface	56.25	063	07:03:23	07:09:59	20:31:50[e]	SC-RTP	4 bit, 8 Msps L1/E1, 400 ms 4 bit, 24 Msps L5, 400 ms
73_0	Surface	61.86	073	10:09:45	N/A	N/A	SC	4 bit, 8 Msps L1/E1, 2000 ms 4 bit, 24 Msps L5/E5a, 2000 ms
74_0	Surface	61.90	073	12:47:17	12:54:22	12:44:57^{+1}	SC-RTP	4 bit, 8 Msps L1/E1, 500 ms 4 bit, 24 Mbps L5/E5a, 500 ms
76_0	Surface	62.20	074	13:07:27	13:21:42	15:05:09^{+1}	SC-RTP	4 bit, 8 Msps L1/E1, 2000 ms 4 bit, 24 Msps L5/E5a, 2000 ms
77_0	Surface	62.42	075	15:12:30	15:17:53	17:55:09[e]	SC-RTP	4 bit, 8 Msps L1/E1, 300 ms
77_1	Surface	62.44	075	19:15:04	19:20:26	21:58:55	SC-RTP	4 bit, 8 Msps L1/E1, 300 ms
78_0[f]	Surface	62.45	075	22:04:02	N/A	N/A	SC	4 bit, 8 Msps L1/E1, 300 ms
78_1[f]	Surface	62.45	075	22:11:28	22:16:51	22:50:32[e]	SC-RTP	4 bit, 8 Msps L1/E1, 300 ms

[a] Altitude (RE) refers to the distance of the lander from the Earth geoid at the operation start time.
[b] SC start time is reported from the IQS packet header.
[c] RTP start and end times are reported from LOG messages. $^{+1}$ indicates that the time refers to the following day.
[d] The operation did not produce GNSS data, as the HGA was intentionally not Earth-pointed.
[e] Aborted operations are associated with a final timestamp power-off.
[f] The operation was performed on receiver RXB.

TABLE 9
Catalog of Main PVT Fixes Across the Entire Mission, Along with Associated Satellite Visibility and DOP Metrics

OP ID	Day of Year	UTC Start	UTC End	Min #Sat	Avg #Sat	Max #Sat	% MultiConst.	% NAV	Min GDOP	Avg GDOP	Max GDOP
1_0	015	15:53:19	16:16:25	4	7.49	9	100%	100%	44.53	54.3	143.84
2_0	016	1:48:19	2:23:57	4	4.75	6	99.86%	100%	148.3	542.11	11247.32
5_0	019	5:43:32	5:49:49	4	4.16	5	100%	100%	1939.33	2059.72	2180.71
9_0	025	5:24:49	5:26:50	4	4	4	100%	100%	459.55	468.31	479.98
14_0	030	23:30:19	23:38:32	4	5.87	7	91.7%	100%	395.13	993.32	7585.77
17_0	034	9:47:46	9:55:52	4	4.13	5	100%	96.92%	2439.87	12915.62	283060.04
21_0	038	23:38:49	0:03:26	4	4.1	5	100%	100%	943.25	3406.21	18712.29
38_0	062	6:51:35	7:25:55	4	4	4	100%	94.08%	39.12	20418.47	413843.19
38_0	062	9:28:50	9:36:04	4	4	4	100%	100%	9706.98	12684.48	16944.52
38_0	062	11:22:24	11:29:59	4	4	4	100%	100%	3385.04	3648.99	3821.23
38_0	062	13:07:50	13:10:42	4	4	4	100%	89.02%	15907.77	31946.46	118398.51
38_0	062	13:21:20	13:25:26	4	4	4	100%	100%	3923.75	4282.65	4567.93
38_0	062	14:48:50	15:01:42	4	4.4	5	100%	99.87%	5115.88	13613.23	26266.35
38_0	062	15:23:20	15:26:39	4	4	4	100%	100%	14268.04	14787.29	15321.61
38_0	062	19:22:42	19:23:21	4	4	4	100%	100%	9772.91	11080.67	15666.69
38_0	062	19:39:02	19:50:57	4	4	4	100%	85.47%	45.79[a]	62625.69	12183166.78
38_0	062	20:17:50	20:34:08	4	4	4	100%	87.59%	57.18[a]	35690.82	548035.24
38_0	063	3:30:03	3:33:24	4	4	4	100%	100%	7168.59	7442.91	7956.91
38_0	063	3:54:42	3:55:11	4	4	4	100%	33.33%	730.25[a]	1553553.96	14658683.18
38_0	063	5:53:51	5:55:44	4	4	4	100%	98.25 %	20834.49	369263.99	5855175.73
40_0	063	8:53:50	8:55:21	4	4	4	100%	100%	11503.36	13604.87	16253.95
40_0	063	12:17:32	12:22:43	4	4	4	100%	99.04%	12167.82	18590	31224.85
40_0	063	12:31:50	12:37:30	4	4	4	100%	100%	9229.29	13025.07	20877.64
40_0	063	17:53:51	18:08:13	4	4	5	100%	100%	6635.51	10857.52	11373.51
74_0	073	15:30:46	15:33:57	4	4	4	100%	100%	1994.65	2163.49	2501.48
74_0	073	19:07:24	19:08:16	4	4	4	100%	100%	2477.27	2519.92	3069.45
74_0	073	19:17:50	19:22:12	4	4	4	100%	99.62 %	10607.25	14925.44	19388.99
74_0	074	0:50:20	0:51:28	4	4	4	100%	100%	6486.85	6633.2	6818.26
74_0	074	3:06:12	3:08:43	4	4	4	100%	100%	5802.9	7817.72	8520.99
74_0	074	3:12:02	3:21:57	4	4	4	100%	99.83%	13109.54	16300.17	20058.89
74_0	074	4:33:50	4:51:25	4	4.18	5	100%	99.91%	6883.68	14838.86	31975.6
74_0	074	5:58:14	6:06:34	4	4	4	100%	100%	6930.72	9428.14	17170.14
74_0	074	6:23:50	6:39:32	4	4	4	100%	50.48%	44.91[a]	87296.94	1174759.19
76_0	074	13:33:02	13:51:28	4	4	4	100%	100%	4964.55	5278.3	5603.77
76_0	074	15:30:42	15:41:31	4	4	4	100%	91.85%	32614.77	39098.46	48082.86
76_0	075	6:41:50	7:22:08	4	4.39	5	100%	95.29%	4851.6	21961.65	49108.64
76_0	075	7:47:25	8:10:27	4	4	4	100%	54.37%	83595.81	111707.1	194658.07
76_0	075	11:53:44	11:58:43	4	4	4	100%	100%	14745.9	14878.66	15013.41
77_0	075	15:46:14	15:52:31	4	4	4	100%	97.62%	28683.46	34636.08	42312.43
77_1	075	20:53:50	21:23:50	4	4.45	5	100%	95.84%	9638.73	18278.77	142204.24
77_1	075	21:50:50	21:51:20	4	4	4	100%	90.32%	52107.47	59902.35	69473.3
78_1	075	22:43:44	22:50:31	4	4	4	100%	97.3%	22302.52	31357.78	55425.92

[a] Unrealistically small DOP values are due to misrepresentation of payload data owing to a numerically ill-conditioned design matrix.